1032

Figure 5 Time-dependent profiles of platelet aggregation by a laser-scattering aggregometer PA-200 after mixing PRP (240 μl) with the polyplexes (60 μl) or the micelles (60 μl); (a) BPEI polyplexes (N/P = 5, 10); (b) P[Asp(DET)] polyplexes (N/P = 5, 10, 20, 40); (c) PEG-b-P[Asp(DET)] micelle (N/P = 5, 10, 20, 40) and (d) 10 mM Tris-HCl buffer (pH 7.4). The vertical values are expressed as the LSI, the unit of which is milli volts (mV). In each figure, the blue, green and red profiles correspond to the aggregates classified as 'small', 'medium' and 'large' (see Materials and methods section), respectively (Min, minute).

described in the Materials and methods section. BPEI and P[Asp(DET)] polyplexes showed an appreciable increase in the LSI of 'small', 'medium' and 'large' category at any N/P ratios (Figure 5a and b), suggesting the significant platelet aggregation. In contrast, PEG-b-P[Asp(DET)] micelle showed no increase in the LSI at any N/P ratios (Figure 5c and d), indicating that the PEG shell of the polyplex micelles effectively prevented the aggregation of platelets.

Erythrocyte aggregation assay

To further study the interaction between the polyplexes and blood cells, erythrocyte aggregation assay was carried out. It is known that erythrocytes possess negative surface charge and interact with positively charged nano-particles, resulting in the aggregate formation.[13] Erythrocytes were harvested from blood of rabbit, followed by washing and suspension with Ringer's solution to avoid the effect of serum proteins. Figure 6 revealed that erythrocytes incubated with BPEI (Figure 6a) and P[Asp(DET)] polyplexes (Figure 6b) underwent aggregation regardless of N/P ratios. By contrast, erythrocytes incubated with PEG-b-P[Asp(DET)] micelle did not undergo any aggregation (Figure 6c), keeping the dispersivity comparable to those in 10 mM Tris-HCl buffer (Figure 6d). These results clearly indicate that neutral and sterically repulsive properties of the polyplex micelle might also effectively prevent

the erythrocyte aggregation through the electrostatic interaction.

Gene transfer to injured rabbit carotid artery

Rabbit carotid artery was injured with a Fogarty balloon catheter to induce neointimal hyperplasia. Twenty-one days later, BPEI (N/P = 10) polyplex, P[Asp(DET)] (N/P = 40) polyplex, and PEG-b-P[Asp(DET)] (N/P = 40) micelle were administered into the carotid artery with neointimal involvement and incubated by cessation of arterial blood flow for 20 min. N/P ratios of the polyplexes and micelles used for in vivo experiments were adjusted to the appropriate values based on the results of in vitro experiments, that is, the balance between the cytotoxicity (Figure 3) and the transfection efficiency (Figure 2). Note that the aggregation assay using albumin (Table 1 and Figure 4), platelets (Figure 5) and erythrocytes (Figure 6) revealed that PEG-b-P[Asp(DET)] micelle had minimal interaction with these biocomponents at any N/P ratios. The entrapped pDNA in the polyplex and the micelle was the expression plasmid vector containing the luciferase gene ($pCAccluc+$). Naked pDNA ($pCAccluc+$) was applied in the same manner as controls. At 3 days after the treatment, the carotid arteries were sampled to assess luciferase activity in each layer of the arterial wall (Figure 7a). All of the rabbits that received naked pDNA ($n = 8$) or the polyplex micelle ($n = 8$) had 100% patency of the carotid artery, whereas considerable

a N/P ratio   5   10

BPEI polyplex

b N/P ratio   5   10

P[Asp(DET)]
polyplex

N/P ratio   20   40

c N/P ratio   5   10

PEG-b-P[Asp(DET)]
micelle

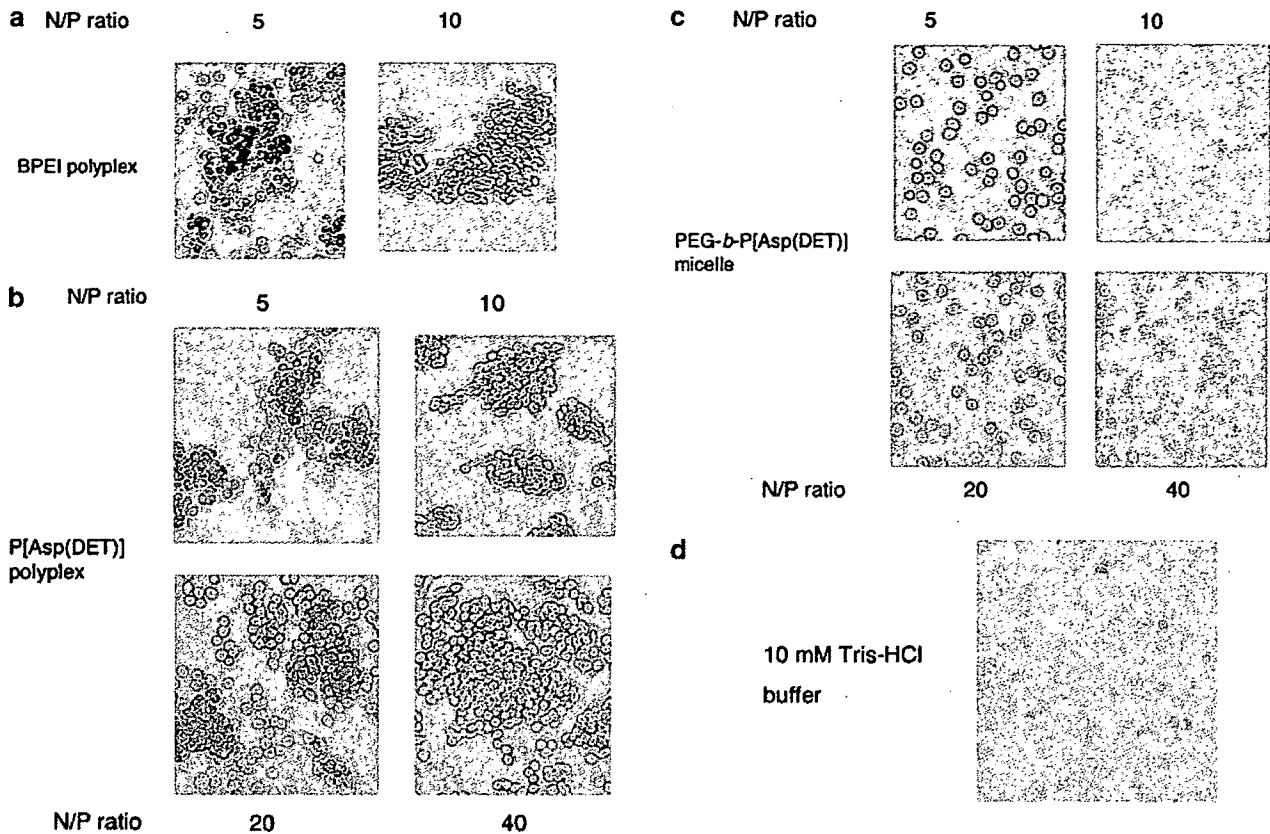N/P ratio   20   40

d

10 mM Tris-HCl

buffer

Figure 6 Photomicrographs of erythrocytes mixed and incubated for 1 h at 37°C with or without polyplexes varying N/P ratios: (a) BPEI polyplex (N/P = 5 and 10); (b) P[Asp(DET)] polyplex (N/P = 5, 10, 20 and 40); (c) PEG-b-P[Asp(DET)] micelle (N/P = 5, 10, 20 and 40) and (d) control in 10 mM Tris-HCl buffer without any polyplexes (control). Aggregation was observed in the medium containing BPEI and P[Asp(DET)] polyplex regardless of N/P ratios, although no aggregation was observed in the medium with PEG-b-P[Asp(DET)] micelle of varying N/P ratio.

thrombo-occlusion of the artery occurred in rabbits in which BPEI (3 occlusions in 8 samples) and P[Asp(DET)] (4 occlusions in 8 samples) polyplexes were applied. The cross sections of the patent and occluded arteries with hematoxylin-eosin stain were shown in Figure 7b–f. The lumens of the occluded arteries challenged with P[Asp(DET)] and BPEI polyplexes were filled with thrombus. All the samples subjected to BPEI polyplex, P[Asp(DET)] polyplex, and PEG-b-P[Asp(DET)] polyplex micelles showed significantly higher luciferase activity in the neointima, media and adventitia than those with naked pDNA. There was no significant difference in the luciferase activity among the samples with BPEI, P[Asp(DET)] and PEG-b-P[Asp(DET)] treatment (Figure 7a).

To confirm in vivo gene transfer to the arterial wall, the expression pDNA containing the FLAG sequence (pMP-FLAG) was then complexed with PEG-b-P[Asp(DET)] and administered to the carotid artery in the same manner. The artery was harvested on day 3, and a cross section of the artery was stained with anti-FLAG antibody. The immunostain clearly showed abundant FLAG-positive cells in the arterial wall, in which FLAG expression was predominantly observed in the neointima (Figure 8a). The pDNA expressing LacZ gene (pCAZ3) was then complexed with PEG-b-P[Asp(DET)] and administered to the carotid artery in the same

manner as negative control. Eventually, the immunostain with anti-FLAG antibody showed no FLAG-positive cells (Figure 8b) in the control specimen.

Discussion

Vascular lesions as feasible targets for gene therapy are generally related to atherosclerosis or its associated diseases. As such lesions develop from the intimal layer of the vascular wall, the intima is a primary target of vascular gene therapy, indicating that delivery via the vessel lumen is the most appropriate approach for efficient gene transfer to vascular lesions. Fortunately, it is easy to approach the luminal surface using a catheter-based method, and several endovascular devices have been developed for this purpose in previous studies. In the vessel lumen, however, attention must be paid to interactions between the gene vector and blood components such as plasma proteins and blood cells. In particular, platelet activation and aggregation promote the coagulant and fibrinolytic pathways through activation of coagulation factors accompanying aggregation of blood cells, resulting in thrombus formation. Most nonviral gene vectors possess a positively charged component in their structure to form a complex with DNA. As blood components ordinarily carry a negative
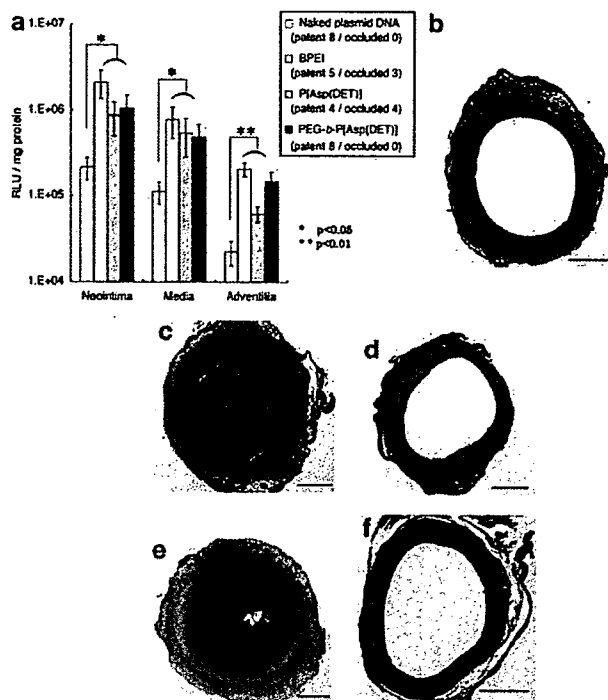
Figure 7 (a) In vivo gene expression evaluated from luciferase activity after intra-arterial delivery of BPEI polyplex (N/P = 10), P[Asp(DET)] polyplex (N/P = 40), and PEG-b-P[Asp(DET)] micelle (N/P = 40). Each polymer was complexed with pCAccluc+ and instilled into the rabbit common carotid artery with neointima. One group of animals was treated with naked pDNA (pCAccluc+) as control. At 72 h, the common carotid artery was excised and luciferase activity was measured. Values are expressed as RLU/mg protein. Values are shown as mean±s.e.m. (*P<0.01, **P<0.05). (b–f) Cross sections of the gene-transferred arteries with hematoxylin-eosin stain, (b) patent, (c) occluded samples of BPEI polyplexes (N/P = 10), (d) patent, (e) occluded samples of P[Asp(DET)] polyplexes (N/P = 40) and (f) patent sample of PEG-b-P[Asp(DET)] micelle (N/P = 40). Bar = 500 μm.
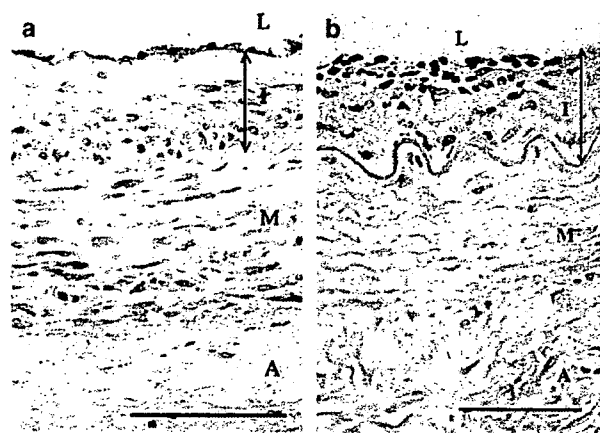

Figure 8 (a) Photomicrographs of rabbit carotid artery transfected with the polyplex micelle composed of pMP-FLAG and PEG-b-P[Asp(DET)] (N/P = 40). (b) Photomicrographs of rabbit carotid artery transfected with the polyplex micelle composed of pDNA expressing LacZ and PEG-b-P[Asp(DET)] (N/P = 40) as control. FLAG-positive region was stained brown. L, lumen; I, intima; M, media; A, adventitia. Bar = 100 μm.

charge, there is a possibility for a nonviral vector to undergo aggregation with plasma proteins and blood cells.[5,13–16] Such aggregation around a gene vector might interfere with the process of gene transfer and also induce thrombus formation, which could worsen the clinical status of the primary disease. Additionally, the positive charge of the gene vector would potentially promote cytotoxic reactions in the lesion and its surrounding part of the vascular wall. As the intima is the most accessible part in vascular gene therapy, as described, the toxic side effects derived from constituent polycations of polyplexes also predominantly appear in the intimal layer of the arterial wall, which might imply injury of intimal cells. In previous studies investigating the mechanisms of atherogenesis, various evidence has been presented to demonstrate that vascular injury is a potent trigger for lesion formation.[17,18] Injury to the vascular wall possibly promotes a variety of responses, such as expression of adhesive molecules and receptors on vascular cells, release of several growth factors, platelet adhesion on the luminal surface and infiltration of inflammatory cells.[19] These responses might influence each other, and potentially induce the formation of neointimal hyperplasia and atherosclerotic lesions. Thus,

minimal vascular injury with biocompatible gene vector systems with low cytotoxicity should be achieved for safe and reliable gene therapy in vascular diseases.

To achieve successful gene delivery to the carotid artery by intravascular method, polyplex micelles, in which the polyplex core is covered with PEG palisades, were used in this study. One of the advantageous characteristics of polyplex micelles with a PEG shell layer is high colloidal stability in a physiological proteinaceous medium, showing reduced interactions with blood components. It was reported that the thrombus formation are caused by nonspecific interaction between blood components and cationic materials such as polyplexes and prosthesis for intravascular application.[13–16,20–24] Srinivasan et al.[20] reported that positively charged prosthetic materials are highly thrombogenic. PEG is the well-known materials with hydrophilic character showing the high biocompatibility and the low thrombogenicity.[25–27] There are previous reports that the surface modification of biomaterials with PEG appreciably reduces thrombogenicity.[25,28–32] Thus, it is widely accepted that PEG shields the cationic surface of biomaterials, reducing their thrombogenicity.[31] In this study, the PEG-b-P[Asp(DET)] micelle system showed no agglomeration even in the presence of blood components including serum albumin (Table 1 and Figure 4), platelets (Figure 5) and erythrocytes (Figure 6), whereas BPEI and P[Asp(DET)] polyplexes definitely showed the aggregate formation due to their positively charged character under the same conditions. It should be noted that PEG-b-P[Asp(DET)] micelle showed no platelet and erythrocyte aggregation even at a high N/P ratios, whereas P[Asp(DET)] and BPEI polyplexes induced platelet and erythrocyte aggregation even at low N/P ratios, such as 5. These results suggest that the surface modification of polyplexes with PEG might prevent their interaction with blood components even at a high N/P ratio required for the effective gene transfection. In addition to the colloidal stability of nonviral vectors with reduced interactions with blood components, another critical issue is the incidence of cytotoxic reactions.

In this regard, the lower cytotoxicity of PEG-*b*-P[Asp(DET)] as compared to BPEI against VSMC, a primary target of vascular gene therapy of atherosclerosis, was demonstrated in Figure 3. Such reduced nonspecific interactions with blood components and low cytotoxicity of polyplex micelles should be the remarkable advantages as the system utilized for *in vivo* nonviral gene delivery via the vascular lumen. Indeed, an *in vivo* study using rabbit carotid artery revealed no occlusion after intraluminal delivery of the polyplex micelle made from PEG-*b*-P[Asp(DET)], whereas the use of polyplexes from BPEI and P[Asp(DET)] resulted in the considerable thrombo-occlusion (Figure 7).

The efficiency of *in vivo* gene transfer is the most important issue in the development of gene vectors for vascular diseases, and the choice of experimental model is crucial for obtaining proper evidence of vascular gene transfer. Experimental studies commonly employ small mammals as animal models, and the artery of such small animals preserves its normal structure even in the adult. In these arteries, because the intima consists of an endothelial monolayer, gene vectors might mainly distribute to the endothelium and medial SMC after administration via the vessel lumen. However, the intimal lesion is the principal target in most vascular gene therapy, and the major cell components of the lesion are intimal SMC and macrophages.[33] Previous studies using an arterial injury model have demonstrated several biological differences between medial SMC and intimal SMC.[33] Also in gene delivery, Guzman *et al*.[34] showed that adenovirus-mediated gene transfer to intimal SMC was highly efficient as compared with that to medial SMC. These findings suggest that the evaluation of vascular gene transfer must be carried out on diseased artery, not normal artery. In the present study, we first induced neointimal hyperplasia in the rabbit carotid artery, and then applied gene vectors to the same artery, which mimicked vascular gene delivery in the clinical setting. Because of the proper preparation of the model, it is expected to provide highly reliable data. In this study, the evaluation using this model showed that gene delivery with the BPEI, P[Asp(DET)], and PEG-*b*-P[Asp(DET)] systems all promoted marked expression of the transferred gene in the neointima, media and adventitia, which was significantly greater than that after the treatment with naked pDNA. In these findings, an interesting feature is that the *in vivo* gene expression level after PEG-*b*-P[Asp(DET)] micelle treatment was similar to that after BPEI or P[Asp(DET)] polyplex treatment (Figure 7a), although the *in vitro* transfection efficiency of the PEG-*b*-P[Asp(DET)] micelle was lower than that of BPEI and P[Asp(DET)] polyplexes (Figure 2). Histological analyses also revealed abundant expression of the marker gene in the arterial wall treated with PEG-*b*-P[Asp(DET)] micelle (Figure 8a), supporting high *in vivo* transfection ability of PEG-*b*-P[Asp(DET)] micelle to vascular lesions. The most likely explanation for such efficient gene transfer to vascular lesions *in vivo* might be an effective buffering action of PEG-*b*-P[Asp(DET)] in the acidic endosomal ·compartment as described previously.[10]

In conclusion, polyplex micelles from PEG-*b*-P[Asp(DET)] showed excellent colloidal stability with reduced nonspecific interactions with blood components and had a unique feature of the lowered *in vitro*

cytotoxicity compared to the conventional polyplexes prepared from BPEI. They achieved efficient gene transfer to the rabbit carotid artery with neointimal hyperplasia without any vascular occlusion, whereas intraluminal delivery of BPEI and P[Asp(DET)] polyplexes induced thrombus formation. Note that the polymerization degree of the polycation segment in the block copolymer is one of the determining factors for the physicochemical property of the polyplex micelles. Block copolymers with relatively shorter polycation segments are not able to form stable polypexes,[35] whereas an increase in the polymerization degree of the polycation segment results in the decreased density of PEG palisades to impair the shielding effect. In this regard, P[Asp(DET)] segment with the polymerization degree of 68 was adopted in this study to construct the block copolymer used in the polyplex micelles, balancing the core stability mainly controlled by the polycation length and the high dispersivity in biological entity correlating mainly with the density of PEG palisades. Eventually, nonspecific interactions with blood components (Table 1, Figures 5 and 6) were effectively shielded, preventing thrombus formation, although achieving appreciable gene transfection, after the intravascular administration (Figure 7). Although there is still an issue of tuning the length of both PEG and P[Asp(DET)] segments in the block copolymer to further optimize the gene transfection and blood compatibility, the concept of the polyplex micelles with the polycation core of low toxicity and high buffering capacity surrounded by the dense PEG palisade was demonstrated to be feasible as nonviral gene vectors useful in the vascular gene therapy.

Materials and methods

Synthesis of block copolymer and homopolymer
The PEG-*b*-P[Asp(DET)] block copolymer (PEG; Mw = 12 000 g/mol, polymerization degree of P[Asp(DET)]; 68) was prepared as described previously.[10] P[Asp(DET)] was synthesized from poly(β-benzyl L-aspartate) (PBLA) by modifying the synthetic method of PEG-P[Asp(DET)]. Briefly, β-benzyl-L-aspartate N-carboxyanhydride was polymerized in N,N-dimethylformamide (DMF)/dichloromethane (1:10) at 40°C by initiation from the primary amino group of *n*-butylamine, followed by acetylation of the N terminus to obtain PBLA. A unimodal molecular weight distribution (Mw/Mn 1.20) of PBLA was confirmed by gel permeation chromatography (columns: TSK-gel G4000HHR+G3000HHR, eluent: DMF+10 mM LiCl, $T = 40$°C, detector: refractive index). The degree of polymerization of PBLA was calculated as 98 from the ^{1}H NMR spectrum (data not shown). Then, the side-chain aminolysis reaction of PBLA was performed by mixing with a 50-fold excess of diethylenetriamine in DMF at 40°C to obtain P[Asp(DET)]. DMF, dichloromethane, and acetic anhydride were purchased from Wako Pure Chemical Industries (Osaka, Japan).

Plasmids
Plasmid *pCAccluc+* was constructed by inserting the recombinant luciferase gene (luc+) into the pCAGGS expression vector. *pCAccluc+* was utilized for all experiments in the present study except morphological

evaluation. Meanwhile, plasmid *pME-FLAG* was constructed by inserting the FLAG tag sequence into the pME expression vector, and used for morphological assessment by immunohistochemical staining. Plasmid *pCAZ3* was constructed by inserting *Escherichia coli* LacZ cDNA into the pCGGGS expression vector. Plasmids were grown in *E. coli* JM109 and purified using Qiagen EndoFree Mega Kits (Qiagen, Hilden, Germany). pDNA was dissolved separately in 10 mM Tris-HCl buffer (pH 7.4), to be 375 µg/ml.

Preparation of polyplex micelle and other polyplexes

Given amounts of PEG-*b*-P[Asp(DET)], P[Asp(DET)] and BPEI were dissolved in Tris-HCl buffer (10 mM, pH 7.40) separately. The concentrations of polymers, PEG-*b*-P[Asp(DET)], P[Asp(DET)] and BPEI were 40, 20 and 5 mg/ml respectively. The polymer solution of PEG-*b*-P[Asp(DET)] was added at varying concentrations and mixed to a 2-fold excess volume of pDNA solution to form polyplex micelles at various N/P ratios. Polyplex micelles were kept overnight before being subjected to evaluation. Polymer with P[Asp(DET)] or BPEI (Mw = 25 kD, Sigma Chemical, MO, USA) was also mixed with pDNA at various N/P ratios to form polyplex. Each polyplex was subjected to evaluation 30 min after mixing.

In vitro gene transfer to VSMC

Human VSMC (Applied Cell Biology Research Institute, WA, USA) were seeded on 24-well culture plates and cultured in 500 µl CS-C medium (Applied Cell Biology) containing 10% serum. When the cells were in a semi-confluent condition, a solution of polyplexes (BPEI and P[Asp(DET)]) or polyplex micelle (PEG-*b*-P[Asp(DET)]) was added to each well (1 µg pDNA/well) (*n* = 4, each). After 24 h of incubation, the cells were washed with PBS and incubated additionally in CS-C for 24 h. N/P ratios of the polyplexes and the micelle were adjusted to 4, 8, 16, 32, 64 and 128. The cells were lysed in 100 µl cell culture lysis reagent (Promega, WI, USA), and luciferase activity of each lysate was quantified using a Luciferase Assay Kit (Promega). The results were expressed as relative light units (RLU) per milligram of total protein measured by bicinchoninic acid assay (Pierce, IL, USA). The experiment was repeated three times.

Cytotoxicity to VSMC

VSMC were seeded into 96-well plates and cultured in 100 µl CS-C. When the cells reached a semi-confluent condition, the polyplexes (BPEI and P[Asp(DET)]) or the micelle (PEG-*b*-P[Asp(DET)]) at various N/P ratios was added to each well (0.25 µg DNA/well) (*n* = 4, each). After 24 h of incubation, the cells were washed, and cultured in CS-C for an additional 24 h. Subsequently, cell viability in each well was evaluated using MTT assay reagent (Dojindo, Kumamoto, Japan) according to manufacturer's instructions. The experiment was repeated three times.

Dynamic light-scattering and laser-Doppler electrophoresis measurements

In dynamic light-scattering (DLS) measurement, the polyplexes, BPEI (N/P = 10) and P[Asp(DET)] (N/P = 40), or the micelle, PEG-*b*-P[Asp(DET)] (N/P = 40), were diluted in 10 mM Tris-HCl buffer (pH 7.4) to adjust the concentration of pDNA to 33.3 µg/ml (*n* = 3, each). DLS measurement was then carried out at 25 ± 0.2°C using a Zetasizer Nano ZEN3600 (Malvern Instruments, Worcestershire, UK) with a vertically polarized incident beam of 488 nm from an Ar ion laser. The scattering angle was fixed at 173°. The data were analyzed by a cumulative method to obtain the hydrodynamic diameter.

Laser-Doppler electrophoresis measurements were performed at 25 ± 0.2°C using a Zetasizer Nano equipped with a He–Ne ion laser (633 nm), and the scattering angle was set at 17° (*n* = 3, each). From the electrophoretic mobility (η), the ζ-potential was calculated using the Smoluchowski equation as follows: $\zeta = 4\pi\eta v/\varepsilon$, where v is the viscosity and ε the dielectric constant of the solvent. The experiment was performed twice.

Measurement of platelet aggregation

Fresh blood from Japanese white rabbits (weight, 2.5–3.0 kg; Saitama Rabbitary, Saitama, Japan) was collected and immediately mixed with a 1:9 volume of 3.8% sodium citrate solution. PRP was isolated by centrifugation at the speed of 900 rounds per minute for 11 min at room temperature and collected as the supernatant. BPEI polyplexes (N/P = 5, 10), P[Asp(DET)] polyplexes (N/P = 5, 10, 20 and 40) and PEG-*b*-P[Asp(DET)] micelles (N/P = 5, 10, 20 and 40) were diluted in 10 mM Tris-HCl buffer (pH 7.4) to adjust the concentration of pDNA to 200 µg/ml. As a negative control, PRP in 10 mM Tris-HCl buffer (pH 7.4) without polyplexes were also used.

Aggregation of platelets in PRP with polyplexes or micelles was evaluated by a laser-scattering aggregometer PA-200 (Kowa). This instrument was reported to sensitively detect small aggregates consisting of only dozens of platelets formed under weak agonists.[36–39] The LSI was measured with the PA-200 to evaluate the existence and the extent of aggregates. According to the default configuration of the PA-200, the LSI was categorized to 'small', 'medium' and 'large' corresponding, respectively, to the small aggregates (9–25 µm), medium aggregates (26–50 µm) and large aggregates (51–70 µm). The results were recorded on a two-dimensional graph showing the time-dependent changes in the LSI. These experiments were repeated three times, and the representative data were shown as the results.

Erythrocyte aggregation assay

Fresh blood from Japanese white rabbits (weight, 2.5–3.0 kg; Saitama Rabbitary) was collected and immediately mixed with 20 µl heparin sodium. Erythrocytes were washed three times and suspended in Ringer's solution. Washed erythrocyte suspension (800 µl) was mixed with polyplex solution (400 µl) and incubated for 1 h at 37°C. BPEI polyplexes (N/P = 5 and 10), P[Asp(DET)] polyplexes (N/P = 5, 10, 20 and 40) and PEG-*b*-P[Asp(DET)] micelles (N/P = 5, 10, 20 and 40) were subjected to the measurement. They were all diluted in 10 mM Tris-HCl buffer (pH 7.4) to adjust the concentration of pDNA to 200 µg/ml. As a negative control, erythrocytes in 10 mM Tris-HCl buffer (pH 7.4) without polyplexes were also prepared. Aggregation of erythrocytes was evaluated under the optical microscope (Olympus, Tokyo, Japan).

1037

Animal model and evaluation of gene transfer efficiency

All animal experiments conformed to the Guide for Care and Use of Laboratory Animals by the US National Institutes of Health (NIH Publication No. 85–23, revised 1996). Japanese white rabbits (weight, 2.5–3.0 kg; Saitama Rabbitary) fed a normal diet were anesthetized by intramuscular injection of xylazine (2.5 mg/kg) and ketamine (50 mg/kg). A 2 Fr Fogarty balloon catheter (Baxter Healthcare, CA, USA) was introduced through the first branch of the left external carotid artery and passed into the left common carotid artery. The balloon was inflated at physiological pressure and passed through the common carotid artery three times with constant rotation. At 21 days after balloon injury, proximal sites of the common carotid artery and internal carotid artery were clamped, and the left common carotid artery was filled with the polyplexes, BPEI (N/P = 10) and P[Asp(DET)] (N/P = 40), or the micelle, PEG-b-P[Asp(DET)] (N/P = 40), through the external carotid artery. In all experiments, each common carotid artery received 400 μl pDNA containing solution (200 μg/ml, 80 μg pDNA). After 20 min incubation, the vector solution was flushed out for washing, and then the arterial circulation was restored. As control, one group of rabbits was treated with naked pDNA (80 μg pCAccluc+) solution in the same manner. Three days later, animals were sacrificed. Evans blue (1 ml of 5% solution) was injected intravenously to mark the neointimal layer of the artery 10 min before sacrificing the animals. Then the left common carotid artery was excised and the connective tissue around the excised artery was removed, and the artery was opened longitudinally. Under a stereomicroscope, blue-stained neointima was first isolated from the artery, and then the elastic medial layer was separated from the adventitia. Each obtained sample was homogenized and lysed in 200 μl cell culture lysis reagent, and luciferase activity of each lysate was measured as described. Gene transfer efficiency was presented as the ratio of luciferase activity to the protein content. The results were expressed as RLU/mgtotal protein.

Immunohistochemical study

To evaluate the distribution of gene expression after gene transfer with PEG-b-P[Asp(DET)] micelles, pME-FLAG was complexed with PEG-b-P[Asp(DET)] (N/P = 40) and applied to rabbit carotid artery in the same manner. Three days after gene delivery, rabbits were sacrificed and subjected to perfusion fixation with 4% phosphate buffered paraformaldehyde (0.1 mol/l PO$_4$ buffer, pH 7.3). The carotid arteries were excised and embedded in paraffin. Cross sections (4 μm) were immunostained with a monoclonal antibody against FLAG tag (1:100, Sigma), as described previously. As a negative control, the cross sections, where PEG-b-P[Asp(DET)] (N/P = 40) micelle with LacZ gene (pCAZ3) was instilled, were stained with anti-FLAG tag antibody.

Statistical analysis

All values are shown as mean$\pm$s.e.m. of biological experiments. The data of in vivo luciferase activity were shown as RLU/mg protein, analyzed by unpaired Student's t-test and considered significant at $P < 0.05$.

Acknowledgements

References

1 Taniyama Y, Tachibana K, Hiraoka K, Namba T, Yamasaki K, Hashiya N et al. Local delivery of plasmid DNA into rat carotid artery using ultrasound. Circulation 2002; 105: 1233–1239.

2 Nishikage S, Koyama H, Miyata T, Ishii S, Hamada H, Shigematsu H. In vivo electroporation enhances plasmid-based gene transfer of basic fibroblast growth factor for the treatment of ischemic limb. J Surg Res 2004; 120: 37–46.

3 Edelstein ML, Abedi MR, Wixon J, Edelstein RM. Gene therapy clinical trials worldwide 1989–2004 – an overview. J Gene Med 2004; 6: 597–602.

4 Tomanin R, Scarpa M. Why do we need new gene therapy viral vectors? Characteristics, limitations and future perspectives of viral vector transduction. Curr Gene Ther 2004; 4: 357–372.

5 Wagner E, Ogris M, Zauner W. Polylysine-based transfection systems utilizing receptor-mediated delivery. Adv Drug Deliv Rev 1998; 30: 97–113.

6 Oupicky D, Konak C, Ulbrich K, Wolfert MA, Seymour LW. DNA delivery systems based on complexes of DNA with synthetic polycations and their copolymers. J Control Release 2000; 65: 149–171.

7 Ogris M, Brunner S, Schuller S, Kircheis R, Wagner E. PEGylated DNA/transferrin-PEI complexes: reduced interaction with blood components, extended circulation in blood and potential for systemic gene delivery. Gene Ther 1999; 6: 595–605.

8 Oupicky D, Konak C, Dash PR, Seymour LW, Ulbrich K. Effect of albumin and polyanion on the structure of DNA complexes with polycation containing hydrophilic nonionic block. Bioconjug Chem 1999; 10: 764–772.

9 Katayose S, Kataoka K. Water-soluble polyion complex associates of DNA and poly(ethylene glycol)-poly(L-lysine) block copolymer. Bioconjug Chem 1997; 8: 702–707.

10 Kanayama N, Fukushima S, Nishiyama N, Itaka K, Jang W-D, Miyata K et al. A PEG-based biocompatible block catiomer with high buffering capacity for the construction of polyplex micelles showing efficient gene transfer toward primary cells. ChemMedChem 2006; 1: 439–444.

11 Harada-Shiba M, Yamauchi K, Harada A, Takamisawa I, Shimokado K, Kataoka K. Polyion complex micelles as vectors in gene therapy – pharmacokinetics and in vivo gene transfer. Gene Therapy 2002; 9: 407–414.

12 Behr JP. The proton sponge. A trick to enter cells the viruses did not exploit. Chimia 1999; 51: 34–36.

13 Kircheis R, Wightman L, Schreiber A, Robitza B, Rossler V, Kursa M et al. Polyethyleneimine/DNA complexes shielded by transferrin target gene expression to tumors after systemic application. Gene Therapy 2001; 8: 28–40.

14 Chonn A, Semple S, Cullis P. Association of blood proteins with large unilamellar liposomes *in vivo*. Relation to circulation lifetimes. *J Biol Chem* 1992; **1111**: 239–246.

15 Dash PR, Read ML, Barrett LB, Wolfert MA, Seymour LW. Factors affecting blood clearance and *in vivo* distribution of polyelectrolyte complexes for gene delivery. *Gene Therapy* 1999; **6**: 643–650.

16 Kircheis R, Wagner E. Polycation/DNA complexes for *in vivo* gene delivery. *Gene Therapy Regul* 2000; **1**: 95–114.

17 Koyama H, Olson NE, Dastvan FF, Reidy MA. Cell replication in the arterial wall: activation of signaling pathway following *in vivo* injury. *Circ Res* 1998; **82**: 713–721.

18 Koyama H, Olson NE, Reidy MA. Cell signaling in injured rat arteries. *Thromb Haemost* 1999; **82**: 806–809.

19 Clinton SK, Libby P. Cytokines and growth factors in atherogenesis. *Arch Pathol Lab Med* 1992; **116**: 1292–1300.

20 Srinivasan S, Sawyer PN. Role of surface charge of the blood vessel wall, blood cells, and prosthetic materials in intravascular thrombosis. *J Colloid Interface Sci* 1970; **32**: 456–463.

21 Kataoka K, Akaike T, Sakurai Y, Tsuruta T. Effect of charge and molecular structure of polyion complexes on the morphology of adherent blood platelets. *Makromol Chem* 1978; **179**: 1121–1124.

22 Kataoka K, Tsuruta T, Akaike T, Sakurai Y. Biomedical behavior of synthetic polyion complexes toward blood platelets. *Makromol Chem* 1980; **181**: 1363–1373.

23 Seaman GV. Plasma protein interactions at biological interfaces. *Thromb Res* 1983; **(Suppl 5)**: 83–91.

24 Ogris M, Steinlein P, Kursa M, Mechtler K, Kircheis R, Wagner E. The size of DNA/transferrin-PEI complexes is an important factor for gene expression in cultured cells. *Gene Therapy* 1998; **5**: 1425–1433.

25 Mori Y, Nagaoka S, Takiuchi H, Kikuchi T, Noguchi N, Tanzawa H *et al*. A new antithrombogenic material with long polyethylene oxide chains. *Trans Am Soc Artif Intern Organs* 1982; **28**: 459–463.

26 Merrill EW, Salzman EW. Polyethylene oxide as a biomaterial. *ASAIO J* 1983; **6**: 60–64.

27 Llanos GR, Sefton MV. Does polyethylene oxide possess a low thrombogenicity? *J Biomater Sci Polym Ed* 1993; **4**: 381–400.

28 Amiji M, Park K. Prevention of protein adsorption and platelet adhesion on surfaces by PEO/PPO/PEO triblock copolymers. *Biomaterials* 1992; **13**: 682–692.

29 Llanos GR, Sefton MV. Immobilization of poly(ethylene glycol) onto a poly(vinyl alcohol) hydrogel: 2. Evaluation of thrombogenicity. *J Biomed Mater Res* 1993; **27**: 1383–1391.

30 Espadas-Torre C, Meyerhoff ME. Thrombogenic properties of untreated and poly(ethylene oxide)-modified polymeric matrices useful for preparing intraarterial ion-selective electrodes. *Anal Chem* 1995; **67**: 3108–3114.

31 Du H, Chandaroy P, Hui SW. Grafted poly(ethylene glycol) on lipid surfaces inhibits protein adsorption and cell adhesion. *Biochim Biophys Acta* 1997; **1326**: 236–248.

32 Pasche S, Voros J, Griesser HJ, Spencer ND, Textor M. Effects of ionic strength and surface charge on protein adsorption at PEGylated surfaces. *J Phys Chem B* 2005; **109**: 17545–17552.

33 Stary HC, Blankenhorn DH, Chandler AB, Glagov S, Insull Jr W, Richardson M *et al*. A definition of the intima of human arteries and of its atherosclerosis-prone regions. A report from the Committee on Vascular Lesions of the Council on Arteriosclerosis, American Heart Association. *Circulation* 1992; **85**: 391–405.

34 Guzman RJ, Lemarchand P, Crystal RG, Epstein SE, Finkel T. Efficient and selective adenovirus-mediated gene transfer into vascular neointima. *Circulation* 1993; **88**: 2838–2848.

35 Itaka K, Yamauchi K, Harada A, Nakamura K, Kawaguchi H, Kataoka K. Polyion complex micelles from plasmid DNA and poly(ethylene glycol)-poly(L-lysine) block copolymer as serum-tolerable polyplex system: physicochemical properties of micelles relevant to gene transfection efficiency. *Biomaterials* 2003; **24**: 4495–4506.

36 Ozaki Y, Satoh K, Yatomi Y, Yamamoto T, Shirasawa Y, Kume S. Detection of platelet aggregates with a particle counting method using light scattering. *Anal Biochem* 1994; **218**: 284–294.

37 Yamamoto T, Egawa Y, Shirasawa Y, Ozaki Y, Sato K, Yatomi Y *et al*. A laser light scattering *in situ* system for counting aggregates in blood platelet aggregation. *Meas Sci Technol* 1995; **6**: 174–180.

38 Tomida Y, Iino S, Nishikawa M, Hidaka H. A new system to detect native microaggregates of platelets *in vivo*, with a novel platelet aggregometer employing laser light scattering. *Thromb Res* 1998; **92**: 221–228.

39 Misawa Y, Konishi H, Fuse K. Platelet aggregates and cardiopulmonary bypass. *Ann Thorac Surg* 2001; **72**: 981–982.

A Protein Nanocarrier from Charge-Conversion Polymer in Response to Endosomal pH

Yan Lee,[†] Shigeto Fukushima,[‡] Younsoo Bae,[†,§] Shigehiro Hiki,[‡,‖] Takehiko Ishii,[#] and Kazunori Kataoka[*,†,‡,§,‖,#]

Division of Clinical Biotechnology, Center for Disease Biology and Integrative Medicine, Graduate School of Medicine, Department of Materials Engineering, Center for NanoBio Integration, CREST, Japan Science and Technology Corporation, and Department of Bioengineering, University of Tokyo, 7-3-1 Hongo, Bunkyo-ku, Tokyo 113-0033, Japan

Received February 14, 2007; E-mail: kataoka@bmw.t.u-tokyo.ac.jp

Smart polymers, whose characteristics change in response to an external signal, such as electric potential, magnetic field, temperature, light, and pH, etc., are spotlighted in various research fields including analytical chemistry, tissue engineering, and drug delivery.[1] Especially, the smart polymers, which are sensitive to biosignals, that is, reductive potential[2] or pH, are very attractive in the drug delivery field requiring selective controlled-release. Some pH-sensitive polymers are even facilitating the endosomal escape of drugs by a membrane interaction and/or an increase in the local osmotic pressure.[3]

pH-Sensitive polymers developed so far that release drugs in the endosomal component use acetal, hydrazone, and orthoester bonds, etc.[4] Although they showed a selective degradation in the endosome, their drug release in response to pH was relatively passive and slow. A more active and prompt response to a small pH drop is needed for more effective drug delivery, for example, the specific release in the early endosome.

Citraconic anhydride is an α-methyl derivative of maleic anhydride, which can be used to mask the charge of proteins. As shown in Scheme 1, amide bonds are formed from the reaction between primary amines and citraconic anhydride. The resulting amides have negative charges owing to the carboxylate groups at the end. The citraconic amide is stable at both neutral and basic pH, but it becomes unstable at acidic pH and promptly degrades back into the cationic primary amine. It has been reported that the citraconic amide degrades around pH 5.[5] Therefore, we considered that the citraconic amide could provide a pH-dependent degradability to the polymers that can be selectively functionalized during the early endosome in a cell. Because the degradation was directly related to the charge-conversion, it could also provide an abrupt change in the interaction with counter-ions.

In this study, we synthesized a block copolymer with combtype side groups of the citraconic amide and characterized their physicochemical properties such as the degree of degradability and the charge conversion. With this polymer, we also developed a novel nanocontainer that can promptly release its protein cargo by generating a repulsive electrostatic force owing to the charge-conversion at the endosomal pH.

The synthesis of the diblock copolymer, poly(ethylene glycol)-poly[(N′-citraconyl-2-aminoethyl)aspartamide] (PEG-pAsp(EDA-Cit)) (4) is illustrated in Scheme 1. The diblock copolymer 2 was synthesized as previously reported.[6] Briefly, the ring-opening polymerization of β-benzyl-L-aspartate N-carboxy-anhydride (BLA-

Scheme 1. Synthesis of PEG-pAsp(EDA-Cit): (a) BLA-NCA/DMF; (b) Ethylenediamine/DMF; (c) Citraconic Anhydride (or Succinic Anhydride)/pyridine
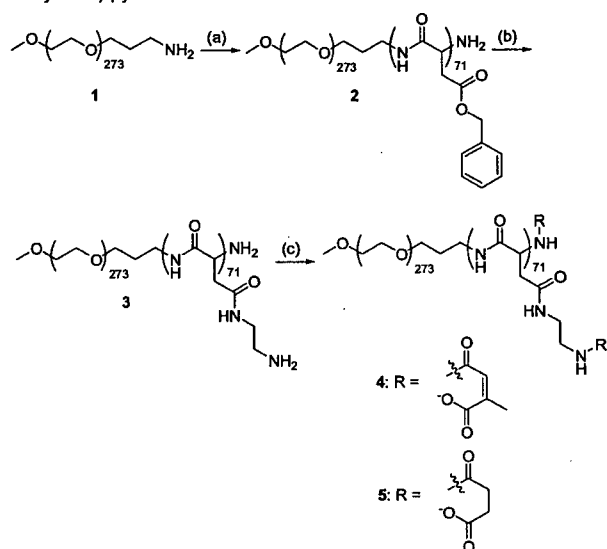
NCA) was initiated by the terminal primary amino group of α-methoxy-ω-amino poly(ethylene glycol) (M_n = 12 000) (1), and the reaction produced 2. The prepared 2 was further modified into PEG-poly[(2-aminoethyl)aspartamide] (3) by aminolysis with excess ethylenediamine. Finally, 4 was synthesized from 3 and the citraconic anhydride in the pyridine solvent. The detailed synthetic procedures are described in the Supporting Information.

The pH-dependent degradation rates of the citraconic amide of 4 are shown in Figure 1. The degradation rate was calculated by measurement of the primary amine concentration in the polymer at 37 °C. The fluorescamine method was used for the quantification of the amine concentration.[7] In the meantime, PEG-pAsp(EDA-Suc) (5) was synthesized as the negative control by mixing 4 with succinic anhydride instead of citraconic anhydride. Although 5 has a structure similar to 4, 5 does not degrade under acidic pH conditions. The experiments showed that approximately 80% of the citraconic amides was degraded in the acetate buffer (pH 5.5) within 1 h, while 60% of the citraconic amides remained intact in the phosphate buffer (pH 7.4) even after 5 h. No degradation was observed in the case of the succinic amides under both pH conditions.

We previously reported that the formation and characterization of the PIC micelles between the PEG-polyaspartate (PEG-pAsp) and lysozyme, of which the isoelectric point occurs at pH 10.[8]

† Center for Disease Biology and Integrative Medicine, University of Tokyo.
‡ Department of Materials Engineering, University of Tokyo.
§ Center for Nanobio Integration, University of Tokyo.
‖ CREST, Japan Science and Technology Corporation.
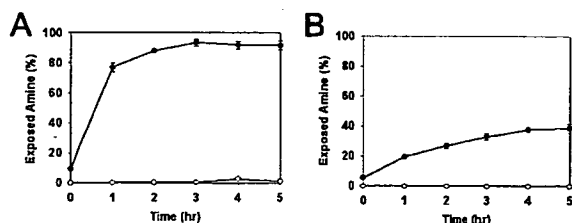# Department of Bioengineering, University of Tokyo.

Figure 1. The degradation of citraconic amide (●) and succinic amide (O) in 4 and 5 at pH 5.5 (A) and pH 7.4 (B). The data are expressed as mean values (± standard deviation) of three experiments.
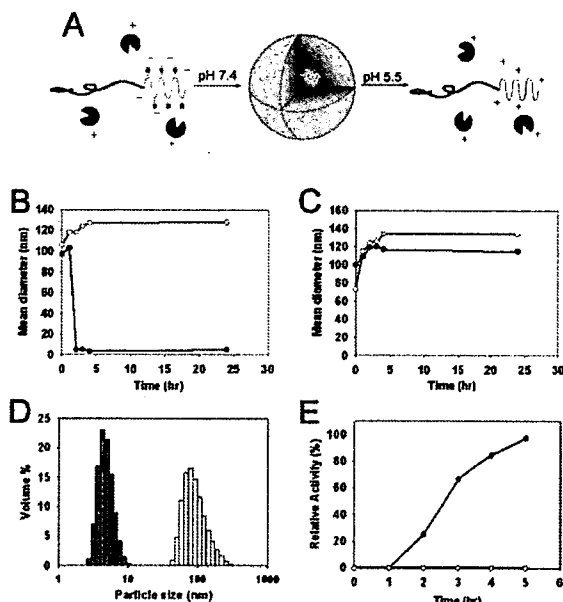

Figure 2. Formation and dissociation of the PIC micelles: (A) schematic diagram for the formation and dissociation of the PIC micelles; the time course of the mean diameter of the PIC micelles of (B) PEG-pAsp(EDA-Cit) and (C) PEG-pAsp(EDA-Suc); (D) the DLS histogram of the PIC micelles at 0 h (white) and at 2 h (gray) at pH 5.5; and (E) the relative lysozyme activity of the PIC micelles. The black dots (●) represent the data at pH 5.5 and the white dots (O) are at pH 7.4.

Following the experimental protocols, the PIC micelles were prepared by mixing 4 and the lysozyme. The pH-dependent stability of the micelles was analyzed by dynamic light scattering (DLS) measurements. The measurements demonstrated that the PIC micelles were successfully formed. More notably, it also suggested that these micelles would be destabilized at the endosomal pH by the degradation of the citraconic amides in 4 accompanied by the charge conversion from negative to positive (Figure 2A).

Figure 2B demonstrates that the size of the micelles prepared from 4 and the lysozymes was stabilized with a diameter of about 130 nm at pH 7.4 even after incubation at 37 °C for 24 h. However, the PIC micelles were promptly dissociated at pH 5.5 within 2 h. The pH dependent profiles of the PIC micelles from 5 and the lysozymes are shown in Figure 2C. As expected, the succinic amide-based micelles were stable at both pH values after 24 h. Figure 2D shows the size distribution of the citraconic amide-based micelles before and after the dissociation. The micelles showed a unimodal size distribution before the dissociation. The distribution around 4.8 nm after a 2-hr incubation resulted from the single lysozyme molecule.[8]

Figure 2E shows the activity of the lysozyme released from the PIC micelles. The lysozyme activity was measured by the well-

known method using the *Micrococcus luteus* cell suspension.[9] The relative activity is expressed as a percentage of the free-lysozyme activity. Because the activity depends on the pH, the free-lysozyme activity at each pH was used for the calculation of relative activity.

At pH 7.4, no lysozyme activity was observed for over 5 h. However, at pH 5.5, the PIC micelles showed a lysozyme activity after 2 h, and it increased and reached 97% of the free-lysozyme activity after 5 h. Interestingly, it took 3 h more to observe the full lysozyme activity after the dissociation of the micelles. Considering the fact that the micelles dissociated within 2 h, it is suggested that there is a weak interaction between the lysozyme and block copolymer chains at least 3 h after the dissociation of the micelles. Because the direct contact between lysozyme and the bacterial cell wall is required for the full activity, PEG chain bound to lysozyme, even though the binding is very weak, can reduce the lysozyme activity. After 80% degradation, 4 cannot form the PIC micelles with lysozyme, but it can still repress the lysozyme activity below 5% (data not shown). Nevertheless, it was confirmed that the citraconic amide-based micelles can selectively dissociate and release the lysozyme while maintaining its enzymatic activity by responding to the change in pH.

In summary, we synthesized the charge-converting block copolymer using the citraconic amide as a pH-sensitive charge masking group. The citraconic amide-based block copolymer was selectively degraded in response to the endosomal pH and formed PIC micelles with the cationic model protein, that is, the lysozyme. Most notably, the micelles selectively released the active lysozyme promptly by sensing the change in pH corresponding to the acidic conditions in the intracellular endosomal compartments. Therefore, it was concluded that our stimuli-sensitive block copolymers are promising designs for future drug and gene delivery systems.

Supporting Information Available: Materials and methods, the temperature-depending degradation rate of the polymer and dissociation rate of the PIC micelles. This material is available free of charge via the Internet at http://pubs.acs.org.

References

(1) (a) Idota, N.; Kikuchi, A.; Kobayashi, J.; Sakai, K.; Okano, T. *Adv. Mater.* 2005, *17*, 2723−2727. (b) Roy, I.; Gupta, M. N. *Chem. Biol.* 2003, *10*, 1161−1171. (c) Schmaljohann, D. *Adv. Drug Delivery Rev.* 2006, *58*, 1655−1670.
(2) (a) Lee, Y.; Koo, H.; Jin, G.; Mo, H.; Cho, M. Y.; Park, J.; Choi, J. S.; Park, J. S. *Biomacromolecules* 2005, *6*, 24−26. (b) Miyata, K.; Kakizawa, Y.; Nishiyama, N.; Harada, A.; Yamasaki, Y.; Koyama, H.; Kataoka, K. *J. Am. Chem. Soc.* 2004, *126*, 2355−2361.
(3) (a) Oishi, M.; Kataoka, K.; Nagasaki, Y. *Bioconjugate Chem.* 2006, *17*, 677−688. (b) Boussif, O.; Lezoualc'h, F.; Zanta, M. A.; Mergny, M. D.; Scherman, D.; Demeneix, B.; Behr, J. P. *Proc. Natl. Acad. Sci. U.S.A.* 1995, *92*, 7297−7301.
(4) (a) Murthy, N.; Thng, Y. X.; Schuck, S.; Xu, M. C.; Fréchet, J. M. J. *J. Am. Chem. Soc.* 2002, *124*, 12398−12399. (b) Bae, Y.; Fukushima, S.; Harada, A.; Kataoka, K. *Angew. Chem., Int. Ed.* 2003, *42*, 4640−4643. (c) Heller, J.; Barr, J.; Ng, S. Y.; Abdellauoi, K. S.; Gurny, R. *Adv. Drug Delivery Rev.* 2002, *54*, 1015−1039.
(5) Shetty, J. K.; Kinsella, J. E. *Biochem. J.* 1980, *191*, 269−272.
(6) Fukushima, S.; Miyata, K.; Nishiyama, N.; Kanayama, N.; Yamasaki, Y.; Kataoka, K. *J. Am. Chem. Soc.* 2005, *127*, 2810.
(7) Udenfriend, S.; Stein, S.; Bohlen, P.; Dairman, W.; Leimgruber, W.; Weigele, M. *Science* 1972, *178*, 871−872.
(8) Harada, A.; Kataoka, K. *Macromolecules* 1998, *31*, 288−294.
(9) Harada, A.; Kataoka, K. *J. Am. Chem. Soc.* 1999, *121*, 9241−9242.

JA071090B

Improvement of cancer-targeting therapy, using nanocarriers for intractable solid tumors by inhibition of TGF-beta signaling

Mitsunobu R. Kano, Younsoo Bae, Caname Iwata, Yasuyuki Morishita, Masakazu Yashiro, Masako Oka, Tomoko Fujii, Akiyoshi Komuro, Kunihiko Kiyono, Michio Kaminishi, Kosei Hirakawa, Yasuyoshi Ouchi, Nobuhiro Nishiyama, Kazunori Kataoka, and Kohei Miyazono

This information is current as of March 2007.

Notes:

Improvement of cancer-targeting therapy, using nanocarriers for intractable solid tumors by inhibition of TGF-β signaling

Mitsunobu R. Kano*†‡, Younsoo Bae‡§, Caname Iwata*¶, Yasuyuki Morishita*, Masakazu Yashiro‖, Masako Oka*, Tomoko Fujii*, Akiyoshi Komuro*, Kunihiko Kiyono*, Michio Kaminishi¶, Kosei Hirakawa‖, Yasuyoshi Ouchi†, Nobuhiro Nishiyama§**, Kazunori Kataoka‡§**††, and Kohei Miyazono*‡‡

Departments of *Molecular Pathology, †Geriatrics, ¶Gastrointestinal Surgery, and §Center for Disease Biology and Integrative Medicine, Graduate School of Medicine; **Department of Materials Engineering, Graduate School of Engineering; and ‡Center for Nano-Bio Integration, University of Tokyo, Tokyo 113-0033 Japan; and ‖Department of Surgical Oncology, Osaka City University Graduate School of Medicine, Osaka 545-8585, Japan

Transforming growth factor (TGF)-β plays a pivotal role in regulation of progression of cancer through effects on tumor microenvironment as well as on cancer cells. TGF-β inhibitors have recently been shown to prevent the growth and metastasis of certain cancers. However, there may be adverse effects caused by TGF-β signaling inhibition, including the induction of cancers by the repression of TGF-β-mediated growth inhibition. Here, we present an application of a short-acting, small-molecule TGF-β type I receptor (TβR-I) inhibitor at a low dose in treating several experimental intractable solid tumors, including pancreatic adenocarcinoma and diffuse-type gastric cancer, characterized by hypovascularity and thick fibrosis in tumor microenvironments. Low-dose TβR-I inhibitor altered neither TGF-β signaling in cancer cells nor the amount of fibrotic components. However, it decreased pericyte coverage of the endothelium without reducing endothelial area specifically in tumor neovasculature and promoted accumulation of macromolecules, including anticancer nanocarriers, in the tumors. Compared with the absence of TβR-I inhibitor, anticancer nanocarriers exhibited potent growth-inhibitory effects on these cancers in the presence of TβR-I inhibitor. The use of TβR-I inhibitor combined with nanocarriers may thus be of significant clinical and practical importance in treating intractable solid cancers.

angiogenesis | gastric cancer | molecular targeting therapy | pancreatic cancer

Chemotherapy that uses nanocarriers has been developed to improve the clinical treatment of solid tumors by obtaining high accumulation of drugs in tumor tissues but limited accumulation in normal organs. Doxil (1), a liposomal adriamycin (ADR), is one such drug that has already been used clinically (2). Doxil has exhibited therapeutic effects on some cancers with hypervascular characteristics (3, 4), including Kaposi sarcoma and ovarian cancers. Another promising formulation of nanocarriers is polymeric micelles (5, 6), which are already being used in clinical trials (7, 8).

However, despite the urgent need for effective chemotherapy for intractable solid tumors, including pancreatic adenocarcinoma (9) and diffuse-type gastric carcinoma (10), nanocarriers of any design have not been successful yet in exhibiting significant therapeutic effects on these cancers. Pancreatic cancer is the fourth leading cause of cancer-related death in the United States and the fifth in Japan (9), and the median survival period of patients who suffer from advanced pancreatic adenocarcinoma is still extremely short (≈6 months), despite recent progress in development of conventional chemotherapies (11). Although cancer cells derived from these tumors are sufficiently sensitive *in vitro* to conventional anticancer agents such as ADR (12), most of these agents have failed to exhibit sufficient therapeutic effects *in vivo*, regardless of formulation, whether encapsulated in nanocarriers or not. The theoretical basis of the

specific accumulation of nanocarriers in tumor tissues is leakiness of tumor vessels to the macromolecular agents, termed the "enhanced permeability and retention (EPR) effect," which was demonstrated and named by Maeda *et al.* (13, 14). The major obstacles to treatment of these cancer cells could thus be insufficient EPR effect because of certain characteristics of their cancer microenvironment, including hypovascularity and thick fibrosis (15, 16). However, methods of regulating this effect have not been well investigated.

Transforming growth factor (TGF)-β signaling plays a pivotal role in both the regulation of the growth and differentiation of tumor cells and the functional regulation of tumor interstitium (17). Because TGF-β is a multifunctional cytokine that inhibits the growth of epithelial cells and endothelial cells and induces deposition of extracellular matrix, inhibition of TGF-β signaling in cancer cells and fibrotic components has been expected to facilitate the effects of anticancer therapy. TGF-β binds to type II (TβR-II) and type I receptors (TβR-I), the latter phosphorylates Smad2 and −3. Smad2 and −3 then form complexes with Smad4, translocate into the nucleus, and regulate the transcription of target genes (18). Several small-molecule TβR-I inhibitors have been reported to prevent metastasis of some cancers (19). However, there may be adverse effects of TGF-β inhibition, including potential progression of some cancers because of the repression of TGF-β-mediated growth inhibition of epithelial cells (20).

In this study, we show that administration of the small-molecule TβR-I inhibitor (LY364947) (21) at a low dose, which could minimize the potential side effects of TβR-I inhibitor, can alter the tumor microenvironment and enhance the EPR effect. This effect of low-dose TβR-I inhibitor was demonstrated with two of nanocarriers, i.e., Doxil and a polymeric micelle incorporating ADR (micelle ADR) that we have recently developed (22) [supporting information (SI) Fig. 7]. The present findings strongly suggest that our method, which uses a combination of

A

H & E staining   PECAM-1/ SMA/ nuclei
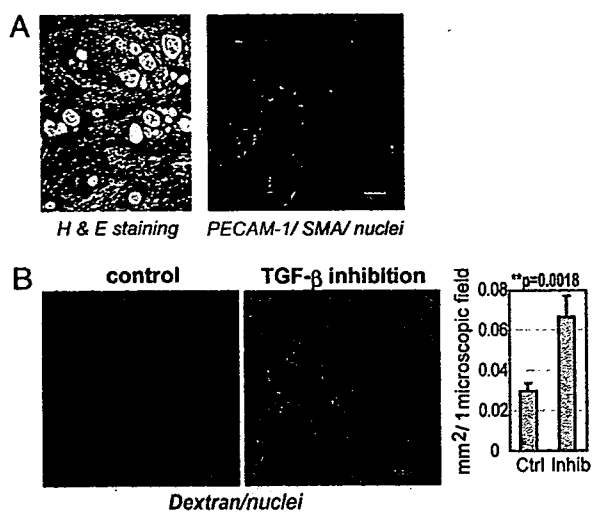
B   control   TGF-β inhibition

Dextran/nuclei

Fig. 1. Histology of BxPC3 xenograft and effects of low-dose TβR-I inhibitor. (A) The histology of the TGF-β-nonresponsive BxPC3 xenograft, used as a model of poorly differentiated pancreatic adenocarcinoma, shown in H&E staining and immunohistochemistry. Examination revealed nests of tumor cells in gland-like structures, with areas rich in fibrotic components (filled by α-smooth muscle actin (SMA)-positive myofibroblasts, shown in red) between them. The tumor tissue also includes some PECAM-1-positive vessels (shown in green) in the interstitium, although almost no vasculature was observed inside the nests of tumor cells. (B) Dextran leakage. At 24 h after administration of low-dose TβR-I inhibitor (1 mg/kg i.p.), i.v.-administered dextran of 2 MDa (50 nm in hydrodynamic diameter) exhibited broader distribution with 1 mg/kg TβR-I inhibitor (Right) than in the control (Left), which was quantified and shown in the graph (n = 12). Error bars in the graphs represent standard errors, and P values were calculated by Student's t test. Ctrl, control; Inhib, inhibitor. (Scale bars, 100 μm.)

low-dose small molecule TβR-I inhibitor and long-circulating nanocarriers, is a promising way to treat intractable cancers.

Results

We used the xenografted BxPC3 human pancreatic adenocarcinoma cell line in nude mice as a disease model (Fig. 1). BxPC3 cells do not respond to TGF-β, because of lack of functional Smad4. Hematoxylin/eosin (H&E) staining of tumor tissue in this model (Fig. 1A Left) revealed poorly differentiated histology, with a certain number of blood vessels and thick fibrotic tissue in the interstitium. There was, however, almost no vasculature inside of tumor cell nests (Fig. 1A Right). This model thus represents the histological characteristics of some intractable solid tumors.

Systemic administration of low-dose TβR-I inhibitor in this model significantly altered the characteristic of tumor vasculature at 24 h after administration. We investigated the functional aspects of the effects of low-dose TβR-I inhibitor, using i.v.-administered large-molecule dextran of 2 MDa with a hydrodynamic diameter of 50 nm (23, 24), which is equivalent to the common sizes of nanocarriers (Fig. 1B). Although dextran of this molecular size for the most part remained in the intravascular space in the control condition, as reported in ref. 24, the use of TβR-I inhibitor resulted in a far broader distribution of this macromolecule around the tumor neovasculature. These findings suggest that low-dose TβR-I inhibitor can maintain blood flow in the tumor vasculature and simultaneously induce extravasation of macromolecules.

To investigate the mechanisms of effect of TβR-I inhibitor on the neovasculature, we analyzed the changes in three major components of tumor vasculature, i.e., endothelium, pericytes (Fig. 2), and basement membrane (SI Fig. 8), at 24 h after
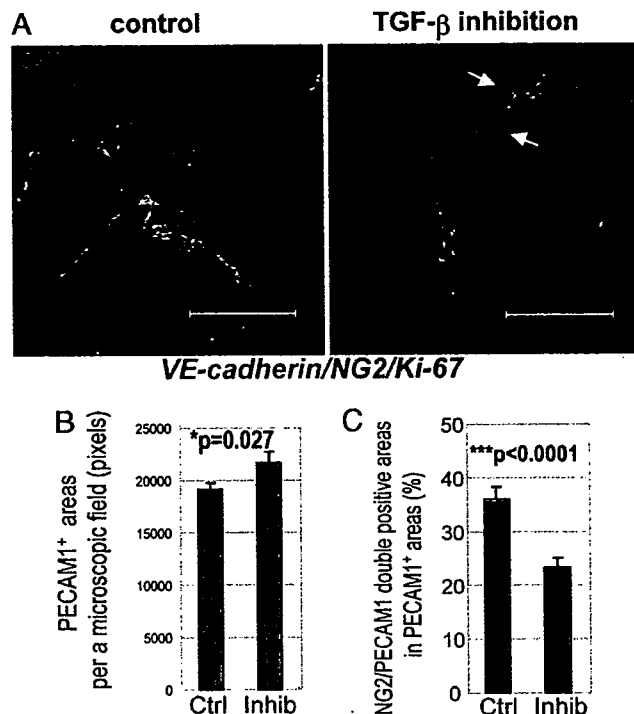

A   control   TGF-β inhibition

VE-cadherin/NG2/Ki-67

B   **C**

Fig. 2. Morphological changes in cancer neovasculature at 24 h after administration of low-dose TβR-I inhibitor. (A) Immunostaining of the tumor neovasculature. NG2-positive pericytes (shown in red) were dissociated (yellow arrows in Right) from VE-cadherin-positive endothelium (shown in green) after TβR-I inhibitor treatment for 24 h. (Scale bars, 50 μm.) (B and C) Areas of PECAM-1-positive endothelium (B) and pericyte-coverage (C) were quantified (n = 40) and are shown in the graphs. Error bars in the graphs represent standard errors, and P values were calculated by Student's t test. Ctrl, control; Inhib, inhibitor.

administration of TβR-I inhibitor. The areas of vascular endothelial cells stained by platelet/endothelial cell adhesion molecule (PECAM)-1 increased slightly with TβR-I inhibitor treatment (Fig. 2B). Although pericyte-coverage of endothelium has been reported to be incomplete in tumors (25), coverage of the endothelium by pericytes, which were determined as NG2-positive perivascular cells, was further decreased by the TβR-I inhibitor treatment. This finding was confirmed by comparing the ratios of PECAM-1/NG2-double-positive areas to PECAM-1-positive areas (Fig. 2C). On the other hand, vascular basement membrane, which was determined by staining with collagen IV, did not differ significantly in the presence or absence of TβR-I inhibitor (SI Fig. 8). We also examined the vasculature in normal organs and found that it was not affected by TβR-I inhibitor in terms of permeability of 2-MDa dextran and morphology on immunostaining (SI Fig. 9).

We next examined the effects of i.p. administration of small-molecule TβR-I inhibitor at a low dose (1 mg/kg) on TGF-β signaling, by determining phosphorylation of Smad2 (SI Figs. 10 and 11). Because it is a small-molecule agent, TβR-I inhibitor transiently suppressed phosphorylation of Smad2. In nucleated blood cells, phosphorylation of Smad2 was significantly suppressed at 1 h after administration of TβR-I inhibitor, but it gradually recovered toward 24 h. In contrast, phosphorylation of Smad2 in tumor cells and most interstitial cells was not suppressed even 1 h after administration, whereas a higher dose (25 mg/kg) of TβR-I inhibitor inhibited Smad2 phosphorylation in most tumor cells. Accordingly, the extent of fibrosis in cancer xenografts treated with low-dose TβR-I inhibitor did not differ
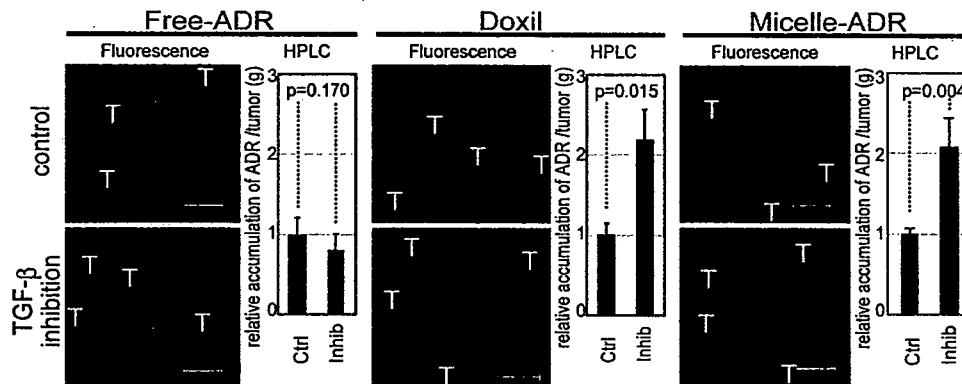
Fig. 3.   Biodistribution of ADR in the BxPC3 model. The biodistribution of ADR was investigated in the BxPC3 model by fluorescence examination (T indicates nests of tumor cells in tumor tissues) and by HPLC. The distributions of Doxil, micelle ADR, and free ADR at 8 mg/kg with and without TβR-I inhibitor at 1 mg/kg were examined 24 h after administration. Enhancement of drug accumulation in tumor was specifically observed with TβR-I inhibitor with Doxil and micelle ADR. Error bars in the graphs represent standard errors, and P values were calculated by Student's t test. Ctrl, control; Inhib, inhibitor.

from that in the control (SI Fig. 12). On the other hand, low-dose TβR-I inhibitor specifically suppressed the phosphorylation of Smad2 in vascular endothelium (SI Fig. 11B). These findings suggest that the use of small-molecule TβR-I inhibitor at low doses is advantageous for limiting adverse effects.

We thus hypothesized that low-dose TβR-I inhibitor may enhance the accumulation of nanocarriers, the molecular sizes of which are similar to 2-MDa dextran, in hypovascular solid tumors. We used two nanocarriers to test this hypothesis: Doxil (26), a liposomal ADR, and a core–shell type polymeric micelle-encapsulating ADR (micelle ADR) that we developed (22). The latter is a micellar nanocarrier consisted of block copolymers in which ADR is conjugated to the PEG chain through an acid–labile linkage. This drug carrier releases free ADR molecules selectively in acidic conditions, e.g., in intracellular endosomes and lysosomes (SI Fig. 7). We tested the effects of i.p. administration of TβR-I inhibitor with i.v. administration of Doxil or micelle ADR at 8 mg/kg on size-matched xenografts of BxPC3 cells, which are ADR-sensitive in vitro (12). Conventional ADR without drug carriers (free ADR), a small-molecule compound of MW 543.52, was also used for comparison. We first examined the distribution of ADR molecules in tumor tissues by using confocal imaging of fluorescence of ADR and HPLC (Fig. 3). The fluorescence of ADR molecules in micelle ADR is detectable only when ADR molecules are released from the micelle, whereas that in Doxil is detectable even when it is encapsulated in the liposome. The total amount of accumulated ADR, the sum of that in cancer cells and the cancer microenvironment, is measured by HPLC, which detects ADR molecules with and without drug carriers. Administration of TβR-I inhibitor with the nanocarriers yielded significant enhancement of intratumoral accumulation of ADR molecules. Because TβR-I inhibitor did not increase the accumulation of free ADR, we suspected that only macromolecules would be benefited by the use of TβR-I inhibitor through enhancement of EPR effect.

We then examined the growth-inhibitory effects of these anticancer drugs with and without TβR-I inhibitor on size-matched BxPC3 xenografts. As shown in Fig. 4A, the growth curves of the BxPC3 xenografts confirmed the findings for the distribution of ADR molecules. None of free ADR, Doxil, micelle ADR as monotherapy, or free ADR with TβR-I inhibitor significantly reduced tumor growth. In contrast, ADR encapsulated in nanocarriers exhibited significant effects on the growth of tumor when combined with TβR-I inhibitor (see SI List for statistical study).

Because micelle ADR was more effective than Doxil (as shown in Figs. 3 and 4A), and the maximum tolerated dose of micelle ADR is far higher than one shot of 8 mg/kg (22, 26) (the dose in Fig. 4A), we further tested the growth-inhibitory effects of an increased dose of micelle ADR combined with TβR-I inhibitor (Fig. 4B). When micelle ADR or free ADR was
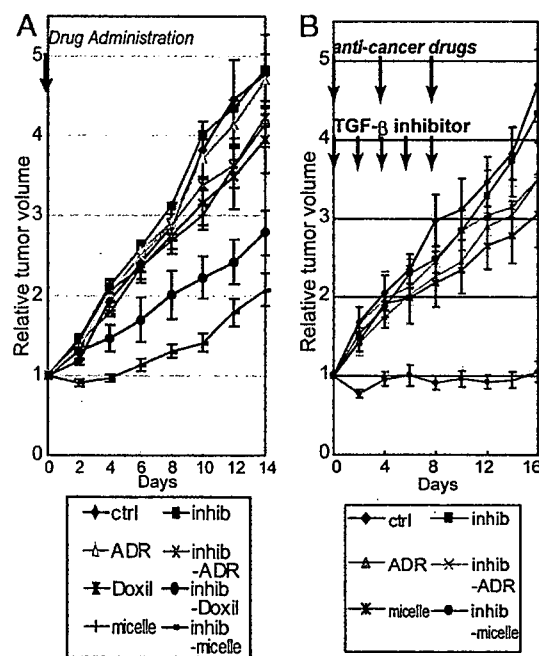

Fig. 4.   Effects of TβR-I inhibitor on anti-tumor activity of nanocarriers, incorporating ADR in the BxPC3 model. (A) Free ADR, liposomal ADR (Doxil), micelle ADR (micelle) or vehicle control (ctrl) was administered i.v. in a single bolus with and without TβR-I inhibitor (inhib) i.p. to xenografted mice in which tumors had been allowed to grow for a few weeks before treatment (n = 5). Relative tumor sizes were measured every second day and are shown as a growth curve with bars showing standard errors. Only nanocarriers administered together with TβR-I inhibitor exhibited significant reduction of growth compared with the control. (B) Growth curve study with an increased dose of micelle ADR. With the day of initiation of drug administration designated day 0, anticancer drugs were administered i.v. on days 0, 4, and 8 with and without i.p. TβR-I inhibitor on days 0, 2, 4, 6, and 8. Further growth-inhibitory effect was observed with an increase in dose of micelle ADR. (Results of multivariate ANOVA study are shown in SI List.)
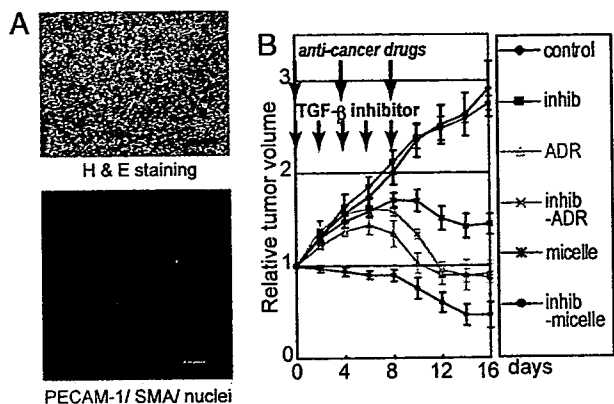
A

H & E staining

PECAM-1/ SMA/ nuclei

B anti-cancer drugs

TGF-β inhibitor

- control
- inhib
- ADR
- inhib-ADR
- micelle
- inhib-micelle

Relative tumor volume

0 4 8 12 16 days

Fig. 5. Growth-curve study in the MiaPaCa-2 pancreatic cancer xenograft model. (A) TGF-β-nonresponsive MiaPaCa-2 cell xenografts exhibited an undifferentiated pattern of histology on H&E staining (*Upper*), with rich SMA-positive fibrotic tissue (show in red in *Lower*) and much less PECAM-1-positive vasculature (shown in green) compared with the BxPC3 model. (B) The same experimental protocol as in Fig. 4B was used in the model, and the effectiveness of the use of TβR-I inhibitor was confirmed. Inhib, inhibitor; micelle, micelle-ADR. (Results of multivariate ANOVA for the growth-curve studies are shown in *SI List.*)

administered on days 0, 4, and 8, with and without TβR-I inhibitor, only micelle ADR administered together with TβR-I inhibitor exhibited nearly complete growth-inhibitory effect on the tumor in this model. We therefore used this regimen in the following experiments.

The efficacy of combined treatment was further confirmed by using micelle ADR in two other animal models of pancreatic adenocarcinoma. We used size-matched xenograft models of MiaPaCa-2 and Panc-1 cell lines, which are both ADR-sensitive *in vitro* (12) (Fig. 5 and SI Figs. 13 and 14). MiaPaCa-2 is nonresponsive to TGF-β signaling because of TβR-II deficiency, whereas Panc-1 has no deficiency in TGF-β signaling components and responds to TGF-β. On histological examination, the xenografts of MiaPaCa-2 and Panc-1 exhibited similar undiffer-

entiated pattern with scattered cancer cells, rich fibrous tissue, and sparse vasculature distributed homogeneously, unlike that of BxPC3 xenografts (Fig. 5A and SI Fig. 14A). Use of low-dose TβR-I inhibitor in these models again significantly enhanced the growth-inhibitory effects of micelle ADR (see Fig. 5B, SI Fig. 14B, and *SI List* for statistical analyses). Effects of free ADR were again not enhanced by TβR-I inhibitor, although the drug itself exhibited some degree of growth-inhibitory effect on the MiaPaCa-2 xenografts. Analysis of the biodistribution of ADR molecules (SI Figs. 13 and 14 C and D) confirmed the effects of TβR-I inhibitor on accumulation of micelle ADR in these cancer models.

We also tested the growth-inhibitory effect of TβR-I inhibitor and micelle ADR in an orthotopic model of the OCUM-2MLN cell line, which responds to TGF-β (27) (Fig. 6). OCUM-2MLN was derived from a patient with another intractable solid tumor, diffuse-type gastric cancer. The cancer cells were implanted in the gastric wall of nude mice and allowed to grow *in situ* for 2 weeks, leading to formation of hypovascular and fibrotic tumors in the gastric wall (Fig. 6A). Tumor area (framed by arrowheads in Fig. 6B, *Left*) was measured before the initiation of drug administration, and tumor growth was evaluated by calculating the relative tumor area at day 16 by measuring tumor area again (Fig. 6B, *Right*). Significant reduction of tumor growth was again observed only in the mice treated with TβR-I inhibitor and micelle ADR. The distribution of ADR, as detected by fluorescence, confirmed this growth-inhibitory effect (data not shown). These findings suggest that the use of TβR-I inhibitor may enhance the accumulation of nanocarriers in hypovascular solid tumors.

Finally, we examined whether low-dose TβR-I inhibitor increases EPR effect specifically in tumor tissues and not in normal organs. Although nanocarriers were originally designed to decrease the drug accumulation in normal organs, it is important to determine whether use of TβR-I inhibitor exacerbates their side effects (SI Fig. 15). In liver, spleen, kidney, blood, and heart, accumulation of ADR as determined by HPLC was not significantly increased by TβR-I inhibitor (SI Fig. 15A and B). Neither dermatitis nor phlebitis around the tail veins was exacerbated by addition of TβR-I inhibitor (SI Fig. 15C). In addition, the weight
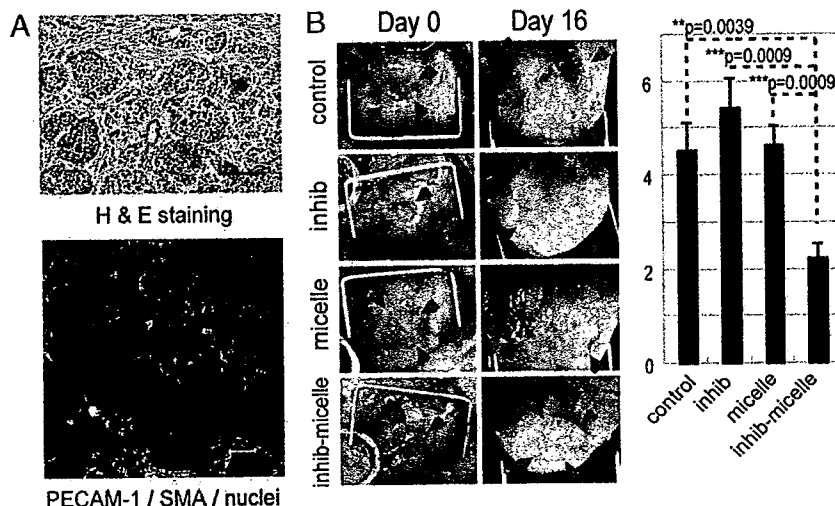

A H & E staining

PECAM-1 / SMA / nuclei

B Day 0   Day 16

control
inhib
micelle
inhib-micelle

**p=0.0039
***p=0.0009
***p=0.0009

control inhib micelle inhib-micelle

Fig. 6. Effects of TβR-I inhibitor administered together with micelle ADR in an orthotopic diffuse-type gastric cancer model. OCUM-2MLN, a human diffuse-type gastric cancer cell line, was inoculated into the gastric wall of nude mice (*n* = 5). Two weeks after inoculation, the cancer tissues exhibited diffuse-type histology on H&E staining (*A Upper*) with sparse formation of blood vessels (PECAM-1 staining, shown in green) (*A Lower*). The sizes of tumors on the gastric wall were measured based on tumor areas (*B Left*), and the values on day 16 were divided by those on day 0, the day of initiation of drug administration, to obtain relative tumor areas. Relative tumor areas are shown with bars for standard errors (*B Right*). TβR-I inhibitor significantly reduced tumor growth in this model, as well. *P* values were calculated by Student's *t* test. Inhib, inhibitor; micelle, micelle-ADR.

of mice that were treated with micelle ADR was not significantly affected by TβR-I inhibitor (data not shown). These findings in normal organs strongly suggest that low-dose TβR-I inhibitor enhances EPR effect only in tumors and that exacerbation of toxicity or side effects of nanocarrier-encapsulated drugs may be minimal with this treatment.

Discussion

In the present study, we have tested a use of TβR-I inhibitor at a low dose to induce alteration in cancer-associated neovasculature to exhibit more leakiness for macromolecules, with less pericyte-coverage and greater endothelial area (Figs. 1 and 2). Because use of TβR-I inhibitor induced the same alteration in neovasculature in the Matrigel plug assay (M.R.K., unpublished data), a model of adult neoangiogenesis (23), the effects of use of TβR-I inhibitor on tumor vasculature observed in the present study may be common in adult neoangiogenesis. Although the roles of growth factors, including TGF-β, may differ during development and in adults, these phenotypes are reminiscent of those of knockout mice deficient in certain components of TGF-β signaling, e.g., endoglin (28, 29), ALK-1 (30, 31), and ALK-5 (32), in which loss of pericyte-coverage and dilatation of the vasculature in yolk sac or embryos were observed. These phenotypes are also consistent with the findings obtained on *in vitro* culture of endothelial cell lineages (33) and mesenchymal progenitor cells (34), which showed that pericyte maturation is promoted, and endothelial proliferation is inhibited, by TGF-β signaling. Vascular phenotypes due to defects in TGF-β signaling *in vivo* are also observed in two types of hereditary hemorrhagic telangiectasia (35, 36), which are induced by deficiencies of endoglin or ALK-1, which are components of TGF-β signaling in vascular endothelium. Because of inborn and life-long abnormality of TGF-β signaling in vasculature, these diseases result in a tendency toward hemorrhage in capillaries that is due to vulnerability of the vascular structure. These observations suggest that use of TβR-I inhibitor at a dose corresponding to that in mice in our study may have similar effects in humans. However, the inhibition of TGF-β signaling is only transient in our method, because of the use of small-molecule inhibitor, and the effects of TβR-I inhibitor may thus be far less severe than the phenotypes observed in hereditary hemorrhagic telangiectasia.

The changes in tumor neovasculature induced by TβR-I inhibitor resulted in enhanced extravasation of molecules, although in a molecular-size dependent manner. Accumulation of 2-MDa dextran with a 50-nm hydrodynamic diameter, Doxil with a 108-nm diameter, and micelle ADR with a 65-nm diameter was enhanced by TβR-I inhibitor in the present study, although accumulation of small-molecule agents, including ADR (MW 543.52) and BrdU (MW 307.10) (M.R.K., unpublished data), was not significantly enhanced. Dreher *et al.* (24) recently reported the molecular-size-dependency of intratumoral drug distribution, using a xenograft model of FaDu cells derived from human hypopharyngeal squamous cell carcinoma. They used several dextrans with molecular sizes ranging from 3.3 kDa to 2 MDa, with estimated hydrodynamic diameters of 3.5 nm to 50 nm, respectively. Dextran molecules of 3.3 kDa and 10 kDa, the smallest ones tested, were found to penetrate deeply and homogeneously into tumor tissue, although they remained in tumor tissue only transiently, for far less than 30 min. However, larger dextran of 2 MDa with a diameter of 50 nm, which we also used in the present study, for the most part remained in the vasculature in cancer tissue and reached only an ≈5-μm distance from the vessel wall at 30 min after injection. Although the histological characteristics of their model, which were not described in their report, may differ from those of the cancer models used in our study, the distribution of 2-MDa dextran observed by Dreher *et al.* agrees with that obtained without TβR-I inhibitor in the BxPC3 xenografts observed in the present study (Fig. 3). TβR-I

inhibitor could thus enhance the accumulation of macromolecules with hydrodynamic diameters of >50 nm, common sizes for nanocarriers, in cancers other than those used in the present study. However, the range of sizes of macromolecules and histological patterns of cancer for which use of TβR-I inhibitor can exhibit enhancing effects remains to be determined.

In conclusion, we have proposed here a use of small-molecule TβR-I inhibitor at a low dose to enhance EPR effect in intractable solid cancers. This method could be a breakthrough in chemotherapy by using nanocarriers in these cancers. Because low-dose TβR-I inhibitor does not affect cancer cells, it may reduce the potential side effects of TGF-β inhibitors, and its enhancing effect is independent of the reactivity of cancer cells to TGF-β signaling. Use of TGF-β inhibitors may thus enable reduction of the systemic doses of nanocarriers and thereby decrease the adverse effects of anticancer drugs.

Methods

TGF-β Inhibitors, Anticancer Drugs, and Antibodies. TβR-I inhibitor was purchased from Calbiochem (San Diego, CA) (LY364947; catalog no. 616451). ADR was obtained from Nippon Kayaku (Tokyo, Japan) and purchased from Kyowa Hakko (Tokyo, Japan). Doxil was purchased from Alza (Mountain View, CA). Micelle ADR was prepared as reported (22) (see *SI Materials and Methods* for detailed information). The antibodies to PE-CAM-1 and VE-cadherin were from BD PharMingen (San Diego, CA), those to neuroglycan 2 and collagen IV were from Chemicon (Temecula, CA), and that to SMA was from Sigma–Aldrich (St. Louis, MO). The anti-phospho-Smad2 antibody was a gift from A. Moustakas and C.-H. Heldin (Ludwig Institute for Cancer Research, Uppsala, Sweden).

Cancer Cell Lines and Animals. BxPC3, MiaPaCa-2, and Panc-1 human pancreatic adenocarcinoma cell lines were obtained from the American Type Culture Collection (Manassas, VA). The OCUM-2MLN human diffuse-type gastric cancer cell line was previously established (27). BxPC3 cells were grown in RPMI medium 1640 supplemented with 10% FBS. MiaPaCa-2, Panc-1, and OCUM-2MLN cells were grown in DMEM with 10% FBS. BALB/c nude mice, 5–6 weeks of age, were obtained from CLEA Japan (Tokyo, Japan), Sankyo Laboratory (Tokyo, Japan), and Charles River Laboratories, (Tokyo, Japan). All animal experimental protocols were performed in accordance with the policies of the Animal Ethics Committee of the University of Tokyo.

Cancer Models. The effects of anticancer drugs were assessed by s.c. implantation of cancer cells into nude mice, and by orthotopic inoculation of OCUM-2MLN cells into the gastric walls of nude mice. A total of 5 × 10⁶ cells in 100 μl of PBS for the xenograft models and the same number in 50 μl of PBS for the orthotopic model were injected into male nude mice and allowed to grow for 2–3 weeks to reach proliferative phase, before initiation of drug administration. For growth-curve studies, the day of initiation of drug administration was considered day 0, and TβR-I inhibitor, dissolved to 5 mg/ml in DMSO and diluted by 100 μl of PBS, or the vehicle control, was injected i.p. at 1 mg/kg on day 0 only in the experiment shown in Fig. 4A and on days 0, 2, 4, 6, and 8 in other experiments. Doxil, micelle ADR, and free ADR at 8 mg/kg, or normal saline as vehicle control, were also administered i.v. in 200 μl/vol via the tail vein on day 0 (Fig. 4A). In other experiments, micelle ADR at 16 mg/kg, free ADR at 8 mg/kg, or normal saline was also administered i.v. on days 0, 4, and 8. There were five mice per group per cell line. The doses of ADR and Doxil were determined based on the lethal doses in mice (22, 26). For biodistribution studies, three mice per group per cell line were treated with 8 mg/kg Doxil, micelle

ADR, or free ADR i.v., with and without TβR-I inhibitor at 1 mg/kg i.p. The mice were examined 24 h after injection.

Quantification in Tumor Models. Xenograft tumors were measured externally every second day until day 16, and tumor volume was approximated by using the equation vol = $(a \times b^2)/2$, where vol is volume, a the length of the major axis, and b is the length of the minor axis. Relative tumor volume was calculated by dividing tumor volume by that on day 0 (the day of initiation of treatment), where actual estimated volumes of xenografted tumors in mm^3 at initiation of drug administration were as follows (mean ± standard error): BxPC3 (in Fig. 4A), 76.4± 7.0; BxPC3 (in Fig. 4B), 74.4 ± 3.3; MiaPaCa-2, 221.2 ± 12.7; and Panc-1, 242.16 ± 24.5. For orthotopic OCUM-2MLN tumors, the area of the primary focus on the gastric wall was measured in Adobe Photoshop software, by opening the abdomen before initiation of treatment and at the end of the observation period. Relative tumor area was calculated by dividing tumor area by that on the day of initiation of treatment. The results were further analyzed statistically by the multivariate ANOVA test, using JMP6 software (SAS Institute, Raleigh, NC).

Histology and Immunohistochemistry. The excised samples were either directly frozen in dry-iced acetone for immunohistochemistry, or fixed overnight in 4% paraformaldehyde and then paraffin-embedded to prepare them for H&E or AZAN staining. Frozen samples were further sectioned at 10-μm thickness in a cryostat, briefly fixed with 10% formalin, and then incubated with primary and secondary antibodies. TOTO-3 for nuclear staining, Alexa488-, Alexa594-, and Alexa647-conjugated secondary antibodies, anti-rat and rabbit IgGs, Zenon labeling kit

anti-rabbit and mouse IgG, and FITC-conjugated dextran (MW 2×10^6) were purchased from Invitrogen Molecular Probes (Eugene, OR). Samples were observed by using a Zeiss (Thornwood, NY) LSM510 Meta confocal microscope for immunohistochemistry, and an Olympus (Tokyo, Japan) AX80 microscope for H&E and AZAN staining.

Biodistribution. Xenografts were inoculated s.c. in nude mice and allowed to grow for 2–3 weeks before drug administration. We then injected TβR-I inhibitor at 1 mg/kg i.p. together with i.v. administration of Doxil, micelle ADR, or free ADR at 8 mg/kg. The tumors or organs were excised 24 h after injection of drugs, and frozen in dry-iced acetone to obtain fluorescence images or weighed and mixed with daunorubicin commensurate with the sample weight as an internal control and then frozen to prepare them for measurement by HPLC. The HPLC method used for analyses is described in ref. 22. To obtain fluorescence images, we performed cryostat sectioning of the frozen samples and washed the sections twice briefly with PBS but did not fix them to avoid elution of ADR. The samples were then observed with a Zeiss confocal microscope, using an excitation laser at 488 nm and a detection filter for the infrared region.

1. Muggia FM (2001) *Curr Oncol Rep* 3:156–162.
2. Ferrari M (2005) *Nat Rev Cancer* 5:161–171.
3. Hassan M, Little RF, Vogel A, Aleman K, Wyvill K, Yarchoan R, Gandjbakhche AH (2004) *Technol Cancer Res Treat* 3:451–457.
4. Emoto M, Udo T, Obama H, Eguchi F, Hachisuga T, Kawarabayashi T (1998) *Gynecol Oncol* 70:351–357.
5. Duncan R (2006) *Nat Rev Cancer* 6:688–701.
6. Kataoka K, Harada A, Nagasaki Y (2001) *Adv Drug Deliv Rev* 47:113–131.
7. Hamaguchi T, Matsumura Y, Suzuki M, Shimizu K, Goda R, Nakamura I, Nakatomi I, Yokoyama M, Kataoka K, Kakizoe T (2005) *Br J Cancer* 92:1240–1246.
8. Nishiyama N, Okazaki S, Cabral H, Miyamoto M, Kato Y, Sugiyama Y, Nishio K, Matsumura Y, Kataoka K (2003) *Cancer Res* 63:8977–8983.
9. MacKenzie MJ (2004) *Lancet Oncol* 5:541–549.
10. Fuchs CS, Mayer RJ (1995) *N Engl J Med* 333:32–41.
11. Burris HA, III, Moore MJ, Andersen J, Green MR, Rothenberg ML, Modiano MR, Cripps MC, Portenoy RK, Storniolo AM, Tarassoff P, et al. (1997) *J Clin Oncol* 15:2403–2413.
12. Watanabe N, Tsuji N, Tsuji Y, Sasaki H, Okamoto T, Akiyama S, Kobayashi D, Sato T, Yamauchi N, Niitsu Y (1996) *Pancreas* 13:395–400.
13. Matsumura Y, Maeda H (1986) *Cancer Res* 46:6387–6392.
14. Maeda H, Matsumura Y (1989) *Crit Rev Ther Drug Carrier Syst* 6:193–210.
15. Sofuni A, Iijima H, Moriyasu F, Nakayama D, Shimizu M, Nakamura K, Itokawa F, Itoi T (2005) *J Gastroenterol* 40:518–525.
16. Takahashi Y, Cleary KR, Mai M, Kitadai Y, Bucana CD, Ellis LM (1996) *Clin Cancer Res* 2:1679–1684.
17. Roberts AB, Wakefield LM (2003) *Proc Natl Acad Sci USA* 100:8621–8623.
18. Feng XH, Derynck R (2005) *Annu Rev Cell Dev Biol* 21:659–693.
19. Bandyopadhyay A, Agyin JK, Wang L, Tang Y, Lei X, Story BM, Cornell JE, Pollock BH, Mundy GR, Sun L-Z (2006) *Cancer Res* 66:6714–6721.
20. Yingling JM, Blanchard KL, Sawyer JS (2004) *Nat Rev Drug Discov* 3:1011–1022.
21. Sawyer JS, Anderson BD, Beight DW, Campbell RM, Jones ML, Herron DK, Lampe JW, McCowan JR, McMillen WT, Mort N, et al. (2003) *J Med Chem* 46:3953–3956.
22. Bae Y, Nishiyama N, Fukushima S, Koyama H, Matsumura Y, Kataoka K (2005) *Bioconjug Chem* 16:122–130.
23. Kano MR, Morishita Y, Iwata C, Iwasaka S, Watabe T, Ouchi Y, Miyazono K, Miyazawa K (2005) *J Cell Sci* 118:3759–3768.
24. Dreher MR, Liu W, Michelich CR, Dewhirst MW, Yuan F, Chilkoti A (2006) *J Natl Cancer Inst* 98:335–344.
25. McDonald DM, Choyke PL (2003) *Nat Med* 9:713–725.
26. Gabizon A, Tzemach D, Mak L, Bronstein M, Horowitz AT (2002) *J Drug Target* 10:539–548.
27. Yashiro M, Chung YS, Nishimura S, Inoue T, Sowa M (1996) *Clin Exp Metastasis* 14:43–54.
28. Li DY, Sorensen LK, Brooke BS, Urness LD, Davis EC, Taylor DG, Boak BB, Wendel DP (1999) *Science* 284:1534–1537.
29. Arthur HM, Ure J, Smith AJ, Renforth G, Wilson DI, Torsney E, Charlton R, Parums DV, Jowett T, Marchuk DA, et al. (2000) *Dev Biol* 217:42–53.
30. Oh SP, Seki T, Goss KA, Imamura T, Yi Y, Donahoe PK, Li L, Miyazono K, ten Dijke P, Kim S, et al. (2000) *Proc Natl Acad Sci USA* 97:2626–2631.
31. Urness LD, Sorensen LK, Li DY (2000) *Nat Genet* 26:328–331.
32. Larsson J, Goumans MJ, Sjostrand LJ, van Rooijen MA, Ward D, Leveen P, Xu X, ten Dijke P, Mummery CL, Karlsson S (2001) *EMBO J* 20:1663–1673.
33. Watabe T, Nishihara A, Mishima K, Yamashita J, Shimizu K, Miyazawa K, Nishikawa S-I, Miyazono K (2003) *J Cell Biol* 163:1303–1311.
34. Hirschi KK, Rohovsky SA, D'Amore PA (1998) *J Cell Biol* 141:805–814.
35. Lebrin F, Deckers M, Bertolino P, ten Dijke P (2005) *Cardiovasc Res* 65:599–608.
36. Fernandez-L A, Sanz-Rodriguez F, Blanco FJ, Bernabeu C, Botella LM (2006) *Clin Med Res* 4:66–78.

Pharmaceutical Nanotechnology

Effective anti-tumor activity of oxaliplatin encapsulated in transferrin–PEG-liposome

Ryo Suzuki [a,1], Tomoko Takizawa [a,1], Yasuhiro Kuwata [a], Mahito Mutoh [a], Nobuyuki Ishiguro [a], Naoki Utoguchi [a], Atsuko Shinohara [b], Masazumi Eriguchi [c], Hironobu Yanagie [c], Kazuo Maruyama [a,*]

[a] *Department of Biopharmaceutics, School of Pharmaceutical Sciences, Teikyo University, 1091-1 Suwarashi, Sagamiko, Sagamihara, Kanagawa 229-0195, Japan*
[b] *Department of Epidemiology and Environmental Health, Juntendo University School of Medicine, 2-1-1 Hongo, Bunkyo-ku, Tokyo 113-8421, Japan*
[c] *Department of Intellectual Property, Research Center for Advanced Science and Technology, The University of Tokyo, 4-6-1 Komaba, Meguro, Tokyo 153-8904, Japan*

Abstract

Oxaliplatin (*trans*-L-diaminocyclohexane oxalatoplatinum, L-OHP) is a novel cisplatin derivative that can improve the side effects of cisplatin such as toxicity to the kidneys and peripheral nerve system. However, L-OHP is effective only when combined with 5-Fluorouracil (5-FU) and Leucovorin. The relatively low anti-tumor index of L-OHP alone is because low levels accumulate in tumor tissues due to high partitioning to erythrocytes *in vivo*. A successful outcome of cancer therapy using L-OHP requires the selective delivery of a relatively high concentration of the drug to tumors. The present study examines tumor-selective delivery of L-OHP using liposomes modified with transferrin-conjugated polyethyleneglycol (TF–PEG-liposomes). Delivery using these liposomes significantly reduced L-OHP partitioning to erythrocytes and improved the circulation time of L-OHP *in vivo*, resulting in enhanced extravasation of liposomes into tumors. The TF–PEG-liposomes maintained a high L-OHP concentration in tumors for over 72 h after intravenous injection, which was longer than that of the liposomes modified with PEG (PEG-liposomes). Intravenously administered L-OHP encapsulated within TF–PEG-liposomes (L-OHP: 5 mg/kg) suppressed tumor growth more effectively than PEG-liposomes, Bare-liposomes and free L-OHP. Although L-OHP is usually combined with 5-FU and Leucovorin, our results suggest that L-OHP encapsulated within TF–PEG-liposomes has potential for cancer therapy.
© 2007 Elsevier B.V. All rights reserved.

Keywords: Liposomes; Transferrin; Oxaliplatin; Targeting; Cancer therapy; Polyethyleneglycol (PEG)

1. Introduction

Surgery, radiotherapy and chemotherapy comprise the current choice of strategies used to fight cancer. However, the present range of anti-cancer drugs does not deliver satisfactory therapeutic effects due to many undesirable side effects.

Cisplatin (*cis*-diamminedichloroplatinum(II)) is one of the most effective agents against testicular, ovarian, head, neck and lung cancers. However, side effects include kidney toxicity, nausea, hearing impairment and irreversible peripheral nerve damage (Durant, 1980). To resolve these issues, considerable effort has been directed towards the development of cisplatin derivatives among which, oxaliplatin (*trans*-L-diaminocyclohexane oxalatoplatinum, L-OHP) has an anti-tumor effect against cisplatin-resistant murine leukemia cells (L1210 cells) (Kidani et al., 1980). L-OHP inhibits DNA synthesis by forming DNA adducts like cisplatin. In addition, it can also inhibit RNA synthesis unlike cisplatin (Tashiro et al., 1989). However, although L-OHP has no renal toxicity (Mathe

et al., 1989; Extra et al., 1990; Machover et al., 1996), its high incidence of adverse drug reactions including peripheral sensory neuropathy and thrombocytopenia remain clinically problematic (Extra et al., 1990). In the FOLFOX4 treatment together with 5-FU and Leucovorin (Rothenberg et al., 2003; Goldberg et al., 2004), L-OHP is a pivotal first line chemotherapeutic agent for treating colon cancer in over 60 countries.

A significant portion of L-OHP in whole blood is sequestered into erythrocytes (Pendyala and Creaven, 1993). The $T_{1/2}$ of L-OHP is 2.3 min (α-phase) and 49 min (β-phase) in mice, and 26 min (α-phase) and 38.7 h (β-phase) in humans. Free L-OHP in the blood is rapidly excreted by the kidneys resulting in the short α-phase, but the high partitioning of L-OHP to erythrocytes is reflected in the long β-phase. To induce the powerful anti-tumor effect of L-OHP, interaction with erythrocytes must be reduced, so that more L-OHP is delivered to tumors for internalization.

We recently described novel target-sensitive liposomes bearing polyethylene glycol (PEG), called pendant-type PEG immunoliposomes, in which antibodies or specific ligands are coupled to the extremities of surface-grafted PEG chains (Maruyama et al., 1995, 1997, 2004; Ishida et al., 2001; Iinuma et al., 2002; Hatakeyama et al., 2004; Kakudo et al., 2004; Miyajima et al., 2006). Functionalized PEG derivatives couple antibodies directly to the distal terminal of PEG chains incorporated in liposomes. We demonstrated that transferrin-coupling pendant-type PEG-liposomes (TF–PEG-liposomes) are effectively extravasated into solid Colon 26 tumors in mice, and internalized into tumor cells (Ishida et al., 2001). The residence time of TF–PEG-liposomes in the circulation is prolonged and reticulo-endothelial system (RES) uptake is low in tumor-bearing mice, resulting in enhanced extravasation of the liposomes into solid tumors. This phenomenon has been characterized as the tumor-selective enhanced permeability and retention (EPR) effect of macromolecules and lipidic particles including liposomes (Matsumura and Maeda, 1986; Ishida et al., 1999). Accumulation in solid tumors is due to the unique vascular characteristics of tumors such as hypervasculature and enhanced vascular permeability, as well as the absence of a lymphatic recovery system (Jain and Gerlowski, 1986; Dvorak et al., 1988). After reaching a tumor site, TF–PEG-liposomes are internalized by receptor-mediated endocytosis and are absorbed into endosome-like intracellular vesicles. The transferrin (TF) receptor concentration on tumor cells is considerably higher than that on normal cells (Wagner et al., 1994). TF receptor-mediated endocytosis is a normal physiological process through which TF delivers iron into cells (Huebers and Finch, 1987; Aisen, 1994). Therefore, the clearance of TF–PEG-liposomes from tumor tissue is so impaired that they remain in the tumor interstitium for prolonged periods (Ishida et al., 2001).

Since selective delivery and cell-entry mechanisms are features of TF–PEG-liposomes, the delivered species of liposome does not need natural affinity for the targeted tumor cells, thus rendering this system potentially applicable to a wide variety of effector molecules, including L-OHP. Here, we examined the potential of liposomes to selectively deliver therapeutic quantities of L-OHP to tumors. We prepared TF–PEG and PEG-liposomes encapsulating L-OHP and compared their tissue distribution in Colon 26 tumor-bearing mice with those of Bare-liposomes and free L-OHP. In addition, we examined the anti-tumor activities of TF–PEG-liposomes encapsulating L-OHP in mice bearing Colon 26 tumors.

2. Materials and methods

2.1. Animals and tumor cells

Six-week-old male BALB/c mice (Tokyo Experimental Animals, Inc., Tokyo, Japan) were maintained at the animal care facility of Teikyo University (Kanagawa, Japan) under a regulated period of light and provided with water and food ad libitum. Colon 26 cells, which are derived from a mouse colon carcinoma, were maintained in RPMI 1640 medium (Sigma–Aldrich Japan, Tokyo) containing 10% fetal calf serum (Gibco, Gaithersburg, MD) under a 5% CO_2 atmosphere at 37 °C.

2.2. Lipids and chemicals

Nippon Oil and Fats Co. (Tokyo, Japan) donated distearoylphosphatidylcholine (DSPC) (COATSOME MC-8080), distearoylphosphatidylethanolamine (DSPE) (COATSOME ME-8080), monomethoxy polyethyleneglycol succinimidyl succinate (PEG-OSu) and polyethyleneglycol bis(succinimidyl succinate) (PEG-2OSu). The number-average molecular weight of PEG(2K)-OSu and of PEG(3K)-2OSu was 2219 and 3230, respectively, and their polydispersity was 1.03 and 1.04, respectively, as measured using gel permeation chromatography. DSPE-PEG(2K) and DSPE-PEG(3K)-COOH were synthesized as described (Maruyama et al., 1995). Cholesterol (CH) and triethylamine were purchased from Wako Pure Chemicals (Osaka, Japan). Human iron-saturated TF was purchased from Sigma (St. Louis, MI) and L-OHP was donated by its developer, Dr. Y. Kidani (Kidani et al., 1980).

2.3. Liposome preparation

Bare-liposomes and PEG-liposomes were prepared from DSPC and CH (2:1, molar ratio) and DSPC, CH, DSPE-PEG(2K) (2:1:0.192, molar ratio), respectively. Small unilamellar vesicles (SUV) of the two types of liposomes were prepared using reverse-phase evaporation (REV). Lipids (300 mg) were dissolved in 4 ml of chloroform/diethyl ether (1:1, v/v) and then 2 ml of 8 mg/ml L-OHP in 9% (w/v) sucrose was dropped into the lipid mixture to form a w/o emulsion. The volume ratio of the aqueous to the organic phase was maintained at 1:2. The emulsion was sonicated for 1 min and then the organic phase was removed to form liposomes by evaporation in a rotary evaporator at 30 °C under vacuum for 1 h. The resulting liposome was extruded through a polycarbonate membrane (100 nm pore size) using an extruder device (Lipex Biomembranes Inc., Canada) maintained at 60 °C to obtain liposomes of a homogeneous size. Unencapsulated free L-OHP was removed by ultracentrifugation at 200,000 × g for 20 min at 4 °C (Hitachi CS120, S100AT5 rotor), and the pellets were resuspended in 9% sucrose.

We prepared TF–PEG-liposomes by coupling TF to PEG-liposomes as described (Ishida et al., 2001). Briefly, 1-ethyl-3-(3-dimethylaminopropyl) carbodiimide (EDC) and N-hydroxysulfosuccinimide (S-NHS) were mixed (DSPE-PEG(3K)-COOH:EDC:S-NHS = 0.067:2.5:6.3, mole ratio) with 1 ml of PEG-liposomes comprising DSPC, CH, DSPE-PEG(2K), DSPE-PEG(3K)-COOH (2:1:0.16:0.032, molar ratio) in MES buffer (10 mM MES in 150 mM NaCl, pH 5.5), and incubated for 10 min at room temperature. The mixture was eluted through a Sephadex G-25 column equilibrated with MES buffer (pH 5.5) and liposome fractions were collected. Various amounts of TF were added to the liposome fractions and gently stirred for 3 h at room temperature. The mixture was centrifuged at 200,000 × g for 20 min at 4 °C, and then the pellet resuspended in 9% sucrose was mixed with $FeCl_3$–nitrilotriacetic acid to yield diferric TF. This suspension was centrifuged at 200,000 × g for 20 min at 4 °C, and the precipitated TF–PEG-liposomes were resuspended in 9% sucrose. The lipid concentration was estimated using a phosphorus assay. Size of liposomes was measured using an electrophoretic light scattering spectrophotometer (ELS-700, Otsuka Electronics, Tokyo) and the L-OHP content was determined using a microwave-induced plasma mass spectrometer (MIP-MS, P-7000, Hitachi, Tokyo) as described below.

2.4. In vitro cytotoxicity

Colon 26 cells (5 × 10³ cells/well) were seeded into 96-well microplates and cultured overnight. Samples were added to each well and the plates incubated for 4 h at 37 °C. The medium was removed and fresh medium was added to each well. After incubation for a further 2 days, cell viability was measured using the WST-1 assay (Cell counting kit, Wako Pure Chemicals, Osaka, Japan).

2.5. Biodistribution in tumor-bearing mice

Tumor-bearing mice were prepared by inoculating a suspension of Colon 26 cells (2 × 10⁶ cells) s.c. into the backs of BALB/c mice. Biodistribution was investigated when the tumors ranged from 6 to 8 mm in diameter. L-OHP solution or L-OHP encapsulated within Bare-, PEG- or TF–PEG-liposomes was injected into the mice via the tail vein. At selected intervals thereafter, the mice were lightly anesthetized, bled via the retro-orbital sinus, then killed by cervical dislocation and dissected. The organs were excised and their L-OHP content was determined using a MIP-MS as described below. Total blood was assumed to comprise 7.3% of the body weight. Contamination with blood in the organs was corrected by examining the distribution of ^{51}Cr-labeled erythrocytes (Maruyama et al., 1993).

2.6. Partitioning of L-OHP into erythrocytes

Samples of blood collected in the presence of anticoagulant (sodium citrate) were centrifuged to obtain plasma and the precipitate containing erythrocytes (erythrocytes fraction). And concentrations of L-OHP were measured at various time points in whole blood, plasma and erythrocyte fraction using a MIP-MS as described below. Data were presented as the percentage of the total injected dose for each sample.

2.7. Quantification of L-OHP

Liposomes, whole blood, plasma, erythrocyte or tissue samples were digested using a programmed microwave procedure. Diluted liposome samples, 20–100 mg of wet tissue or 100 μl of plasma were weighed and placed in PFA vials (Taf-tainer vial, GL Science, Tokyo). Thereafter, 400 μl of concentrated nitric acid and 200 μl of hydrogen peroxide (Tama Pure AA 100, Tama Chemicals, Tokyo) were added and digestion proceeded in a microwave oven (MLS-1200 MEGA; Milestone s.r.l., Italy) as follows; 250 W for 5 min, 0 W for 1 min, 250 W for 5 min, 400 W for 5 min, and 600 W for 5 min. The digested samples were brought to 1.0 ml with milli Q water, and then diluted. The content of L-OHP was measured using a MIP-MS. Europium (Eu) was added to the assay mixture and calibration standards at 0.1% and 20 ng/ml (final concentrations), respectively. The L-OHP concentrations were calculated from ion counts at platinum (Pt) using the calibration method with internal standard correction. The L-OHP concentrations in tissues were expressed as micrograms of L-OHP per gram tissue.

2.8. Measurement of serum albumin, total protein, glutamic–oxaloacetic transaminase (GOT), glutamic–pyruvic transaminase (GPT) and blood urea nitrogen (BUN)

A solution of L-OHP or L-OHP encapsulated within Bare-, PEG- or TF–PEG-liposomes was injected into tumor-bearing mice via the tail vein at a dose of 5 mg L-OHP/kg. Three days later, the mice were anesthetized and blood samples were collected using glass capillaries from the vein of the fundus oculi. Serum obtained from blood samples by centrifugation was tested for albumin, total protein, GOT, GPT and BUN using respective kits (A/G B test Wako for albumin and total protein, GOT-UV Test Wako for GOT, GPT-UV Test Wako for GPT and Urea Nitrogen B Test Wako for BUN, Wako Pure Chemicals, Osaka, Japan).

2.9. Therapeutic effects of L-OHP encapsulated liposomes

A suspension of Colon 26 cells (2 × 10⁶ cells) was inoculated s.c. into the backs of BALB/c mice. Therapeutic effects were examined when the tumors ranged from 8 to 10 mm in diameter. A solution of L-OHP or L-OHP encapsulated within Bare-, PEG- or TF–PEG-liposomes was injected twice into the tumor-bearing mice via the tail vein at a dose of 5 mg L-OHP/kg on days 9 and 12 after tumor cell inoculation. The two perpendicular diameters of tumors were obtained at intervals of a few days using a slide caliper and then tumor volumes were calculated using the formula $0.5\,(A \times B^2)$, where A and B are the longest and shortest dimensions (mm) of the tumor, respectively. Tumor growth ratio was represented as the ratio for the tumor

volume on days 9 (before L-OHP treatment) after tumor cell inoculation.

2.10. Statistical analysis

Differences between PEG-liposomes and TF–PEG-liposomes were compared with unpaired Student's t-test.

3. Results

3.1. Cytotoxicity of L-OHP encapsulated TF–PEG-liposomes

L-OHP was encapsulated within Bare-, PEG- or TF–PEG-liposomes, all measuring about 180 nm in diameter. The amounts of encapsulated L-OHP within the Bare-, PEG- and TF–PEG-liposomes measured by MIP-MS were 12.3, 19.2 and 14.8 μg/mg liposomal lipid, respectively. We initially assessed the cytotoxicity of these liposomes against Colon 26 cells, which overexpress TF receptors, in vitro. Both L-OHP in solution and encapsulated within all three types of liposomes were cytotoxic against Colon 26 cells in a dose-dependent manner (Fig. 1). The ED_{50} values of L-OHP in solution and encapsulated within Bare-, PEG- and TF–PEG-liposomes were 2, 60, 18, and 8 μg/ml for Colon 26 cells, respectively. The L-OHP encapsulated within TF–PEG-liposomes was the most cytotoxic among the three types of the liposomes. In addition, we examined whether the cytotoxicity of L-OHP encapsulated within TF–PEG-liposomes was due to uptake of the liposomes via TF receptor into Colon 26 cells. When liposome uptake via TF receptors was inhibited by adding an excess of TF into medium, the cytotoxicity of L-OHP encapsulated within TF–PEG-liposomes was decreased (Fig. 1). On the other hand, blocking TF receptors did not influence the cytotoxicity of L-OHP encapsulated within PEG-liposomes. These results indicated that TF–PEG-liposomes were internalized into Colon 26 cells via TF receptor-mediated endocytosis and delivered L-OHP into the cytoplasm.

3.2. Biodistribution of L-OHP encapsulated within TF–PEG-liposomes in mice bearing tumors

Liposomes with encapsulated L-OHP were injected i.v. into mice bearing Colon 26 tumors and L-OHP distribution was evaluated. Fig. 2A shows the time course of plasma clearance after the i.v. injection of L-OHP in solution and liposomal L-OHP. The L-OHP in solution was rapidly cleared from the blood circulation whereas the circulation of L-OHP encapsulated within liposomes was increased. The blood concentrations of L-OHP encapsulated within PEG- and TF–PEG-liposomes were much higher than that of L-OHP encapsulated within Bare-liposomes. We also assessed the biodistribution of L-OHP in solution and of L-OHP encapsulated within various liposomes at 6 h after i.v. injection (Fig. 2B). The results showed that very little L-OHP was distributed to the major tissues in mice. In contrast, the distribution of L-OHP encapsulated in PEG- and TF–PEG-liposomes to the liver and spleen differed, but far less of both was distributed to these tissues compared with Bare-liposomes. These results indicated that the PEG layer prolonged the systemic circulation of liposomes after i.v. injection. Thus, the conjugation of TF to the PEG terminal did not alter the RES uptake of PEG-liposomes, presumably because TF is a blood glycoprotein. Furthermore, PEG chains occupying the liposome surface played a role in the prolonged circulation of TF–PEG-liposomes.
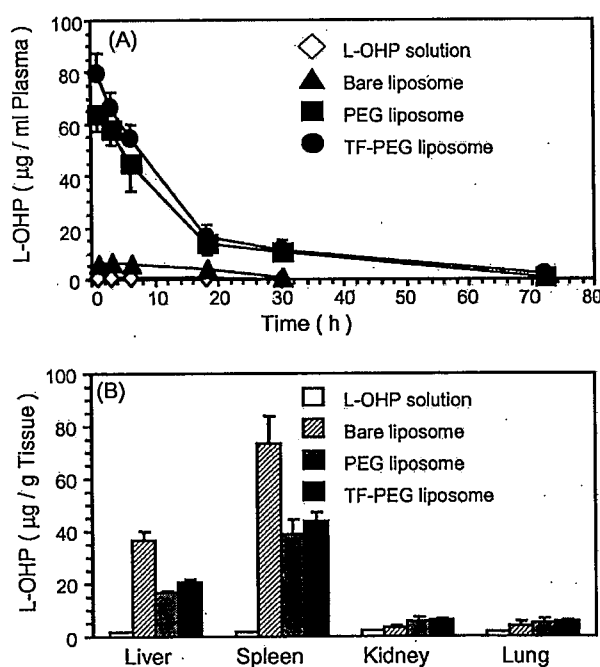
Fig. 2. Plasma clearance (A) and biodistribution (B) of L-OHP solution or liposomal L-OHP in Colon 26-bearing mice. (A) L-OHP in solution or encapsulated within Bare-, PEG- or TF–PEG-liposomes (L-OHP: 5 mg/kg) was injected via tail veins of Colon 26-bearing mice. At various times thereafter, blood samples were collected using glass capillaries from veins of fundus oculi. Plasma L-OHP levels were measured by MIP-MS. (B) L-OHP in solution or encapsulated within Bare-, PEG- or TF–PEG-liposomes (L-OHP: 5 mg/kg) was injected via tail veins of Colon 26-bearing mice. Six hours later, mice were sacrificed and liver, spleen, kidneys and lungs were collected. Concentrations of L-OHP in tissue samples were measured by MIP-MS. Data are shown as means and standard deviation $(n = 3)$.
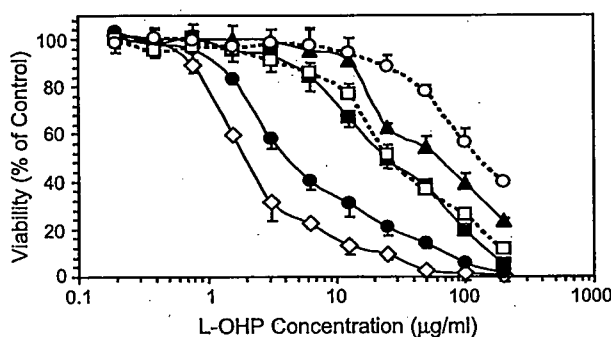
Fig. 1. Cytotoxicity of L-OHP in solution and liposomal L-OHP against Colon 26 cells. Cells were incubated with L-OHP in solution (open diamonds) or encapsulated within Bare- (solid triangles), PEG- (solid squares) or TF–PEG-liposomes (solid circles) without TF, or with PEG- (open squares) or TF–PEG-liposomes (open circles) with TF for 4 h 37 °C under 5% CO_2. Thereafter, cells were washed and incubated with fresh medium for 2 days at 37 °C in 5% CO_2. Cell growth was assayed using WST-1 assay. Maximal cell growth (100%) was obtained by incubating cells without L-OHP. Data are shown as means and standard deviation $(n = 5)$.